

MULTI-RESOLUTION PARAMETER CHOICE METHOD FOR TOTAL VARIATION REGULARIZED TOMOGRAPHY

KATI NIINIMÄKI, MATTI LASSAS, KEIJO HÄMÄLÄINEN, AKI KALLONEN,
VILLE KOLEHMAINEN, ESA NIEMI, AND SAMULI SILTANEN

August 12, 2015

ABSTRACT. A computational method is introduced for choosing the regularization parameter for total variation (TV) regularization. The approach is based on computing reconstructions at a few different resolutions and various values of regularization parameter. The chosen parameter is the smallest one resulting in approximately discretization-invariant TV norms of the reconstructions. The method is tested with X-ray tomography data measured from a walnut and compared to the S-curve method. The proposed method seems to automatically adapt to the desired resolution and noise level, and it yields useful results in the tests. The results are comparable to those of the S-curve method; however, the S-curve method needs *a priori* information about the sparsity of the unknown, while the proposed method does not need any *a priori* information (apart from the choice of a desired resolution). Mathematical analysis is presented for (partial) understanding of the properties of the proposed parameter choice method. It is rigorously proven that the TV norms of the reconstructions converge with any choice of regularization parameter.

CONTENTS

1. Introduction	2
2. The space $BV(D)$: definitions and approximations	6
3. Multi-resolution convergence analysis	13
4. Computational models and algorithms	18
4.1. X-ray attenuation model	18
4.2. Discrete anisotropic TV	19
4.3. Quadratic programming	19
4.4. Primal-dual interior-point (PD-IP) method	20
4.5. The PD-IP algorithm	21
5. Results	21
5.1. X-ray measurement data	21
5.2. Selection of α using the parameter choice rule	22
5.3. Selection of α using the S-curve method	23
6. Discussion and conclusions	26
Appendix A. Construction of the difference matrices	30
Appendix B. A note on BV norms	30
References	31

1. INTRODUCTION

In X-ray tomography one collects projection images of an unknown two- or three-dimensional body from different directions. For each direction, an X-ray source is placed on one side of the body and an X-ray detector on the opposite side. After a calibration step involving a logarithm of the measured projection images, the X-ray tomography experiment can be quite accurately modelled by

$$(1.1) \quad \tilde{\mathbf{g}} = \mathcal{A}u + \mathbf{e},$$

where vector $\tilde{\mathbf{g}} \in \mathbb{R}^M$ is the data and $u : \Omega \rightarrow \mathbb{R}_+$ is the X-ray attenuation function defined in a bounded domain $\Omega \subset \mathbb{R}^n$. In this work, we take Ω to be the unit square $[0, 1]^2$. The operator \mathcal{A} represents integrals over u over the areas or volumes connecting the X-ray source and a pixel in the detector (pencil beam model). See Figure 1(a). Furthermore, $\mathbf{e} \in \mathbb{R}^M$ is a Gaussian random vector modelling measurement noise.

The inverse problem is *given the measurement geometry and noisy data $\tilde{\mathbf{g}}$, recover a discrete approximation $\mathbf{f} \in \mathbb{R}^N$ to u* . Depending on the number and geometry of projection directions, this inverse problem is either mildly or strongly ill-posed [43, 42]. Ill-posedness means high sensitivity to inaccuracies in modelling and to errors in measurement. Overcoming this sensitivity requires *regularization*.

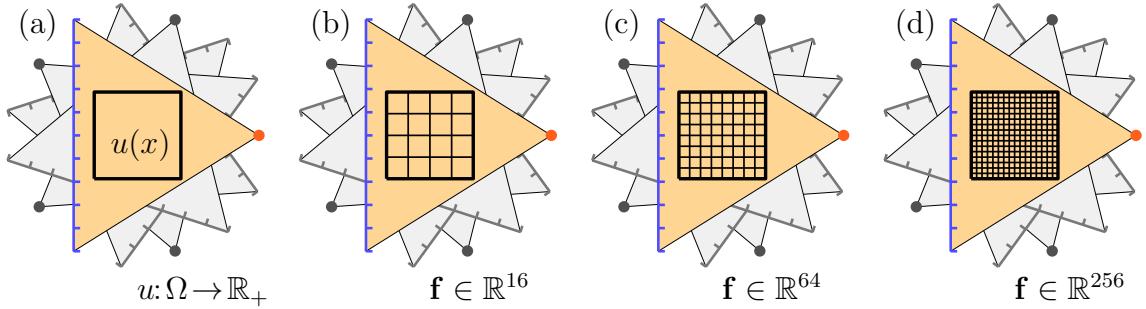


FIGURE 1. Schematic illustration about the relationship between continuous and discrete tomographic models. (a) Continuous model for two-dimensional X-ray tomography. The function $u(x)$ of equation (1.1) gives the point-wise X-ray attenuation coefficient inside the domain Ω shown here as a square. The dots show the five locations of the X-ray source. The detector has 10 pixels, so there is a total of 50 data points. (b-d) Discrete models with various resolutions. The attenuation coefficient is modelled as constant inside each pixel. The point of this figure is to demonstrate how the resolution of our computational model can be freely chosen while number of data points is fixed.

In this work, we study regularizing two-dimensional tomographic problems using Total Variation (TV) regularization introduced in [49]. We need a finite approximation to the continuous measurement model (1.1). Consider the discrete model

$$(1.2) \quad \mathbf{g} = A\mathbf{f},$$

where $\mathbf{f} \in \mathbb{R}^N$ represents the discretized two-dimensional body under imaging. We divide the square Ω into $N = n \times n$ square pixels with side length $1/n$. The function u is approximated by a function which is constant inside each pixel; those pixel values are listed as elements of the vector \mathbf{f} (see Appendix A). Further, $\mathbf{g} \in \mathbb{R}^M$ denotes the measurement data consisting of pixel values in digital X-ray projection images, and $A \in \mathbb{R}^{M \times N}$ is a matrix approximation to \mathcal{A} (see [42, Section 2.3.4]).

The discrete TV-regularized solution is defined by

$$(1.3) \quad \hat{\mathbf{f}}_{\alpha,n} := \arg \min_{\mathbf{f} \in \mathbb{R}_+^N} \left\{ \|A\mathbf{f} - \tilde{\mathbf{g}}\|_2^2 + \frac{\alpha}{n} \sum_{\kappa \sim \kappa'} |f_\kappa - f_{\kappa'}| \right\},$$

where $\alpha > 0$ is a so-called regularization parameter. We use the *anisotropic* definition of total variation: in (1.3) the relation $\kappa \sim \kappa'$ is true whenever elements f_κ and $f_{\kappa'}$ of the vector \mathbf{f} correspond to values at either horizontally or vertically neighboring pixels.

How to choose the regularization parameter α in (1.3)? To our best knowledge, these are all the currently available methods in the literature:

- (1) The classical L-curve method [28].

- (2) Discrepancy principle, introduced for TV regularization by Wen and Chan in [58] in the context of image restoration. This method needs *a priori* information about the measurement noise amplitude.
- (3) Two approaches (quasi-optimality principle and Hanke-Raus rules) described by Kindermann, Mutimbu and Resmerita in [34].
- (4) The so-called *S-curve method*, introduced in [35] and implemented for wavelet-based tomography in [27], can be extended to total variation regularization. Such extension is done in this paper for the first time, making use of *a priori* information about the sparsity of the gradient of the unknown.

There is so far no parameter choice method that would be the best (or even perform acceptably) for *all* applications. Rather, it seems that for any given application there is a quest for finding a method that gives consistent, robust and useful results. For this reason we think that there needs to be a large collection of methods for parameter choice, based on different principles, for scientists and engineers to have a better chance of finding a good option for each practical situation.

We propose a new parameter choice method, based on solving the inverse problem at multiple resolutions. Namely, while the number M of measurement points is fixed (it is simply the number of detector elements times the number of projection images), the number $N = n \times n$ of pixels in the reconstruction can be freely chosen. See Figure 1 for an illustration.

Given a tomographic dataset, we can use definition (1.3) to compute reconstructions in the same square domain but at varying resolutions n . We prove in Section 3 that if we keep $\alpha > 0$ in equation (1.3) fixed and let $n \rightarrow \infty$, then $\hat{\mathbf{f}}_{\alpha,n}$ converges to a limit image. The proof is an extension of the one-dimensional result [38] to dimension two.

We propose the following practical method for choosing the parameter $\alpha > 0$:

Parameter choice method. Given a noisy dataset $\tilde{\mathbf{g}}$, compute $\hat{\mathbf{f}}_{\alpha,n}$ defined by (1.3) for a set of α values and at two or more resolutions n , including the resolution intended for showing the final result. Calculate the discrete TV norms of the reconstructions and define the optimal α to be the smallest value that leads to TV norms that do not depend significantly on n .

At this point we do not claim that the above algorithm is a parameter choice rule in the strict sense as defined in [17]. However, the numerical evidence presented in Section 5 suggests that the method works well and, as expected, leads to larger α when the noise level is increased.

In light of our new theorem, the TV norms of the reconstructions converge for any choice of α as $n \rightarrow \infty$. How exactly can the above approach work at all? It seems that the ill-posedness of the tomography problem shows up as significant n -dependence of the TV norms of reconstructions whenever α is too small to regularize away the instability caused by the term $\|\mathbf{A}\mathbf{f} - \tilde{\mathbf{g}}\|_2^2$. Since the final intended resolution is included in the test resolutions, our choice rule adapts to the relevant resolution and the noise level.

The reader may wonder why α is divided by n in (1.3). The TV regularization formulation for smooth functions takes the form

$$(1.4) \quad \arg \min_{u \geq 0} \left\{ \|\mathcal{A}u - \tilde{\mathbf{g}}\|_2^2 + \int_{\Omega} |\nabla u| dx \right\}$$

to the discrete minimization problem (1.3). The division by n comes from approximations with a finite difference quotient and a midpoint rule integration quadrature:

$$(1.5) \quad \int_{\Omega} \left| \frac{\partial u}{\partial x_1} \right| dx \approx \int_{\Omega} \left| \frac{u(x_1 + \frac{1}{n}, x_2) - u(x_1, x_2)}{\frac{1}{n}} \right| dx \approx \left(\frac{1}{n} \right)^2 \sum_{\kappa \sim \kappa'} \left| \frac{f_{\kappa} - f_{\kappa'}}{\frac{1}{n}} \right|.$$

In (1.5) the relation $\kappa \sim \kappa'$ is true whenever elements f_{κ} and $f_{\kappa'}$ of \mathbf{f} correspond to values at horizontally neighboring pixels. A similar computation using vertical differences is needed as well for the analysis regarding (1.4).

Applying total variation regularization to tomographic problems dates back to 1998 [14] in case of simulated data and to 2003 [36] in case of measured data. Since then, there have been many further studies: [37, 40, 52, 30, 53, 16, 5, 32, 54, 33, 51, 11, 12].

There are many computational approaches for minimizing the total variation regularized least squares functional (1.3). These include quadratic programming [38, 31, 23, 35, 27], lagged diffusivity method [15], domain decomposition methods [22, 21], Bregman distance methods [47, 60, 24, 6, 61], primal-dual methods [9, 8, 18, 44], finite element methods [19, 3], discontinuous Galerkin methods [26] and other methods [39, 56, 57, 25, 7]. See also the books [55, 48, 10, 50, 29]. In this paper we use a primal-dual interior-point quadratic programming method based on dividing the unknown to non-negative and non-positive parts in the spirit of [42, Section 6.2]. One advantage of this approach is natural and effective enforcement of non-negativity of the attenuation coefficient.

Scientific novelties of this paper include

- Proving the convergence of TV reconstructions as the resolution is increased.
- Testing the S-curve method in the context of TV regularized tomography.
- Introducing a novel multi-resolution parameter choice method and testing it with measured X-ray data.

While we discuss here the new multi-resolution parameter choice method for two-dimensional tomographic problems only, the computational approach generalizes directly to three-dimensional settings and other inverse problems as well. However, the convergence proof is currently available only in dimensions one [38] and two (Section 3 below).

2. THE SPACE $BV(D)$: DEFINITIONS AND APPROXIMATIONS

Let D be the square $[0, 1]^2 \subset \mathbb{R}^2$. We use the following anisotropic definition for the space $BV(D)$ of functions of bounded variation defined on D .

Definition 2.1. *The anisotropic space $BV(D)$ consists of functions $u \in L^1(D)$ for which $V(u) < \infty$. Here $V(u)$ is given for smooth functions by*

$$(2.1) \quad V(u) = V(u; D) = \int_D \left(\left| \frac{\partial u(x)}{\partial x_1} \right| + \left| \frac{\partial u(x)}{\partial x_2} \right| \right) dx.$$

For general $u \in BV(D)$, $\left| \frac{\partial u(x)}{\partial x_j} \right|$ in formula (2.1) is defined as total variation of the distributional derivative interpreted as a measure [1]. The BV norm is defined by

$$(2.2) \quad \|u\|_{BV(D)} := \|u\|_{L^1(D)} + V(u; D).$$

We will use two different concepts of weak convergence in the space $BV(D)$.

Definition 2.2. *A sequence $u_j \in BV(D)$ converges weakly in $BV(D)$ to limit u as $j \rightarrow \infty$, that is, $u_j \xrightarrow{BVw} u$, if u_j and their distributional derivatives ∇u_j satisfy*

$$(2.3) \quad \begin{cases} \lim_{j \rightarrow \infty} \|u_j - u\|_{L^1(D)} = 0, & \text{and} \\ \nabla u_j \rightarrow \nabla u \text{ weakly in } \mathbf{M}(D, \mathbb{R}^2) \text{ as } j \rightarrow \infty. \end{cases}$$

Above $\mathbf{M}(D, \mathbb{R}^2)$ denotes \mathbb{R}^2 -valued Borel measures on D . Note that $\mathbf{M}(D, \mathbb{R}^2)$ is the dual space of $C(D; \mathbb{R}^2)$. Recall now from [1, Def. 10.1.3] the definition of another useful type of weak convergence:

Definition 2.3. *Let u_j be a sequence in $BV(D)$ and $u \in BV(D)$. Then u_j converges to u as $j \rightarrow \infty$ in the sense of intermediate convergence if and only if*

$$(2.4) \quad \lim_{j \rightarrow \infty} \|u_j - u\|_{L^1(D)} = 0, \quad \text{and}$$

$$(2.5) \quad \lim_{j \rightarrow \infty} \int_D |\nabla u_j(x)| dx = \int_D |\nabla u(x)| dx.$$

According to [1, Proposition 10.1.2], intermediate convergence of Definition 2.3 implies weak convergence of Definition 2.2.

We need a result on approximating elements of $BV(D)$ by functions that are piecewise constant on square pixels of fine enough resolution. For each $j > 0$, consider the closed dyadic squares

$$(2.6) \quad S_{j, \vec{k}} = S_{j, k_1, k_2} = [k_1 2^{-j}, (k_1 + 1) 2^{-j}] \times [k_2 2^{-j}, (k_2 + 1) 2^{-j}] \subset D,$$

where $0 \leq k_1 \leq 2^j - 1$ and $0 \leq k_2 \leq 2^j - 1$. See Figure 2(b) for an illustration of a dyadic grid formed by such squares. Let $T_j : L^2(D) \rightarrow L^2(D)$ be the orthogonal projections defined by averaging over squares:

$$(2.7) \quad (T_j u)|_{\text{int}(S_{j, \vec{k}})} = \frac{1}{|S_{j, \vec{k}}|} \int_{S_{j, \vec{k}}} u(x) dx.$$

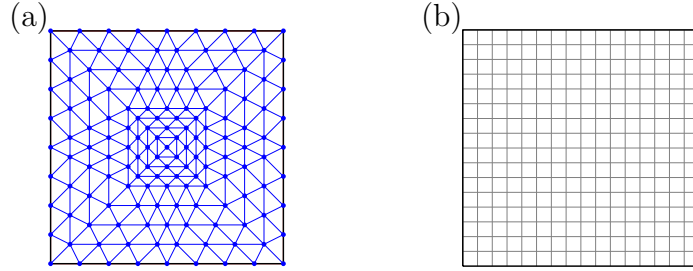


FIGURE 2. Examples of different discretizations of the square domain $D = [0, 1]^2$ used below overlaid in the same square. (a) Finite triangulation. (b) Square grid corresponding to $j = 4$ and $n = 16$.

For any $j > 0$, the set $Y_j := \text{Range}(T_j)$ consists of $L^2(D)$ functions that are piecewise constant in the open squares belonging to the rectangular $2^j \times 2^j$ grid (2.6).

Lemma 2.4. *For all $u \in BV(D)$ and $\varepsilon > 0$ there is $j_1 > 0$ such that there is a v_2 that is piecewise constant in the dyadic $2^{j_1} \times 2^{j_1}$ grid (2.6) and satisfies*

$$\rho_{1,1}(u, v_2) < \varepsilon,$$

where the $\rho_{1,1}$ -distance is defined by

$$(2.8) \quad \rho_{1,1}(u, v) = \|u - v\|_{L^1(D)} + |V(u) - V(v)|.$$

Proof. Let $u \in BV$ and $\varepsilon > 0$. We know from [4] that there is a function v_0 which is piecewise constant in a finite triangularization of D and satisfies

$$(2.9) \quad \rho_{1,1}(u, v_0) < \varepsilon/3.$$

Set $M = \|v_0\|_{L^\infty(D)}$. Let us choose some notation for the concepts related to the fixed triangularization corresponding to v_0 .

- (1) Triangles denoted by $T_\nu \subset D$ with $\nu = 1, 2, \dots, T$.
- (2) Edges of the triangles are line segments $\gamma_\ell \subset D$ indexed by $\ell = 1, 2, \dots, L$.
- (3) Vertices $p_r \in D$ with $r = 1, 2, \dots, R$.
- (4) The minimum distance between two separate vertices is denoted by $\delta_0 > 0$.
- (5) The minimum angle between any two edges sharing an endpoint is called $\alpha_0 > 0$.
- (6) The length of the longest edge is denoted by G .

See Figure 2(a) for an illustration of a finite triangularization.

Next we define *clusters*. Given $j > 1$, let $B'_r = B'_{r,j}$ be union of all the closed squares $S_{j,\vec{k}}$ containing the vertex p_r . See the orange sets in Figure 3. Furthermore, define clusters $B_r = B_{r,j}$ by

$$(2.10) \quad B_r = \bigcup \{S_{j,\vec{k}} \mid S_{j,\vec{k}} \cap B'_r \neq \emptyset\}.$$

Then $p_r \in B'_r \subset B_r$. The clusters are shown in gray in Figures 3, 4 and 7.

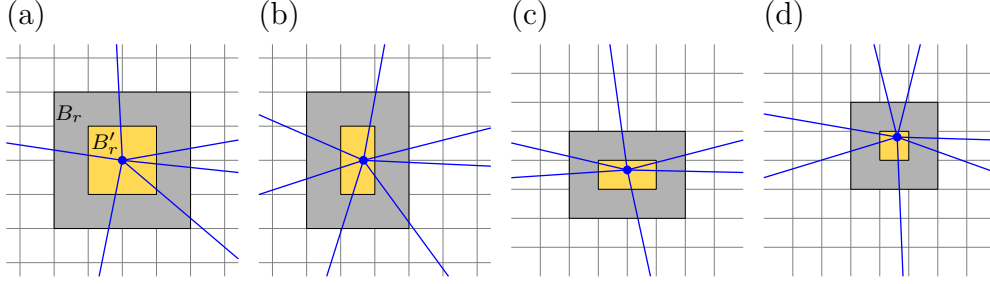


FIGURE 3. Possible positions of a triangle vertex (blue dot) in the dyadic square grid. The triangle edges are shown in blue. The sets B'_r are shown as yellow and the clusters B_r as light gray. (a) vertex at the corner of squares. (b) vertex at a horizontal edge between squares. (c) vertex at a vertical edge between squares. (d) vertex in the interior of a square.

In the following, consider integers j_0 large enough for the following to hold:

$$(2.11) \quad 4\sqrt{2} \cdot 2^{-j_0} < \delta_0.$$

Now (2.11) implies that the sets B_r are disjoint and contain at most one vertex each.

Let v_1 be the function obtained from v_0 by replacing its value in each cluster B_r by 0. Then we have

$$\|v_0 - v_1\|_{L^1(D)} \leq \sum_{r=1}^R \int_{B_r} |v_0 - v_1| dm \leq 16RM(2^{-j_0})^2$$

since each cluster consists of at most 16 squares of area $(2^{-j_0})^2$. Furthermore, the V expression (2.1) can be very simply computed for functions that are piecewise constant with respect to either a finite triangulation or to a square grid. Namely, (2.1) is the sum of (Manhattan distance) lengths of jump curve segments multiplied by the jump in function value over those curve segments. Therefore we can estimate

$$|V(v_0) - V(v_1)| \leq 8LMR2^{-j_0} + 32MR2^{-j_0},$$

where the first term in the right hand side comes from the triangularization. We used the facts that the Manhattan length of any edge restricted inside a cluster is at most $4 \cdot 2^{-j_0}$ and that v_0 can jump at most $2M$ at an edge. The second term in the right hand side comes from the jump of v_1 , bounded by $2M$, at the cluster boundary whose maximal length is $16 \cdot 2^{-j_0}$.

Now we can fix so large j_0 that (2.11) holds and that we have

$$(2.12) \quad \rho_{1,1}(v_0, v_1) < \varepsilon/3.$$

Next we construct tubular neighborhoods. Denote the union of all clusters by

$$\mathcal{B} = \bigcup_{r=1}^R B_r.$$

Note that $\mathcal{B} \subset \mathbb{R}^2$ is a closed set. Further, consider the parts of triangle edges that are outside the clusters:

$$(2.13) \quad \tilde{\gamma}_\ell := \gamma_\ell \setminus \mathcal{B}.$$

For all $\varrho > 0$, define

$$(2.14) \quad \Gamma_{\ell, \varrho} := \{x \in \mathbb{R}^2 \mid \text{dist}(x, \tilde{\gamma}_\ell) < \varrho\} \setminus \mathcal{B},$$

where “dist” refers to Euclidean distance. The sets $\Gamma_{\ell, \varrho}$ are open tubular neighborhoods of $\tilde{\gamma}_\ell$ in $D \setminus \mathcal{B}$. See Figures 4(a) and 5.

We need to determine an upper bound for $\varrho > 0$ ensuring that the sets $\Gamma_{\ell, \varrho}$ are disjoint. It is clear from the construction of the sets B_r and B'_r that (Euclidean) $\text{dist}(p_r, D \setminus \mathcal{B}) > 2^{-j_0}$. As illustrated in Figure 4(a), the minimal angle α_0 between edges determines a lower bound for the distance between the intersection points of two edges with the boundary ∂B_r . A trigonometric consideration shown in Figure 4(b) implies that the tubular neighborhoods $\Gamma_{\ell, \varrho}$ are disjoint whenever ϱ satisfies $0 < \varrho < h_0$ with

$$(2.15) \quad h_0 := 2^{-j_0} \tan \frac{\alpha_0}{2}.$$

See Figure 5 for an illustration of the tubular neighborhoods in a triangulation.

Next we consider refining the square grid outside the clusters as shown in Figure 6. The smaller squares of size $2^{-j_1} \times 2^{-j_1}$ are defined by the formula (2.6) with a large enough $j_1 > j_0$. The idea is to take j_1 so large that we can fit a dyadic polygonal chains inside the tubular neighborhoods as shown in Figure 7(a).

Consider two vertices p_1 and p_2 connected by an edge γ_1 . (There is no loss of generality since we can always renumber the vertices and edges.) Take j_1 so large that

$$(2.16) \quad 2^{-j_1} < \frac{\varrho}{4}.$$

Then we can connect the clusters B_1 and B_2 using a piecewise linear curve

$$c_1 : [0, 1] \rightarrow \bar{\Gamma}_{1, \varrho}$$

with the following properties:

- The edge γ_1 and the dyadic polygonal chain c_1 are disjoint: $\gamma_1 \cap c_1 = \emptyset$.
- The curve starts from the boundary of B_1 and ends at the boundary of B_2 ; in other words $c_1(0) \in \partial B_1$ and $c_1(1) \in \partial B_2$.
- The curve c_1 is close to the edge γ_1 :

$$(2.17) \quad \min_{x \in \gamma_1} \|c_1(t) - x\|_2 < 3 \cdot 2^{-j_1} \text{ for all } t \in [0, 1].$$

- The range $c_1([0, 1])$ of the curve consists of boundary segments of squares belonging to the $2^{-j_1} \times 2^{-j_1}$ grid.
- The curve is injective: if $t_1 \neq t_2$ then $c_1(t_1) \neq c_1(t_2)$.
- The dyadic polygonal approximation c_1 is optimal in the following sense: if $c'_1 : [0, 1] \rightarrow \bar{\Gamma}_{1, \varrho}$ is another curve satisfying all of the above conditions for c_1 , then $\text{length}(c'_1([0, 1])) \geq \text{length}(c_1([0, 1]))$.

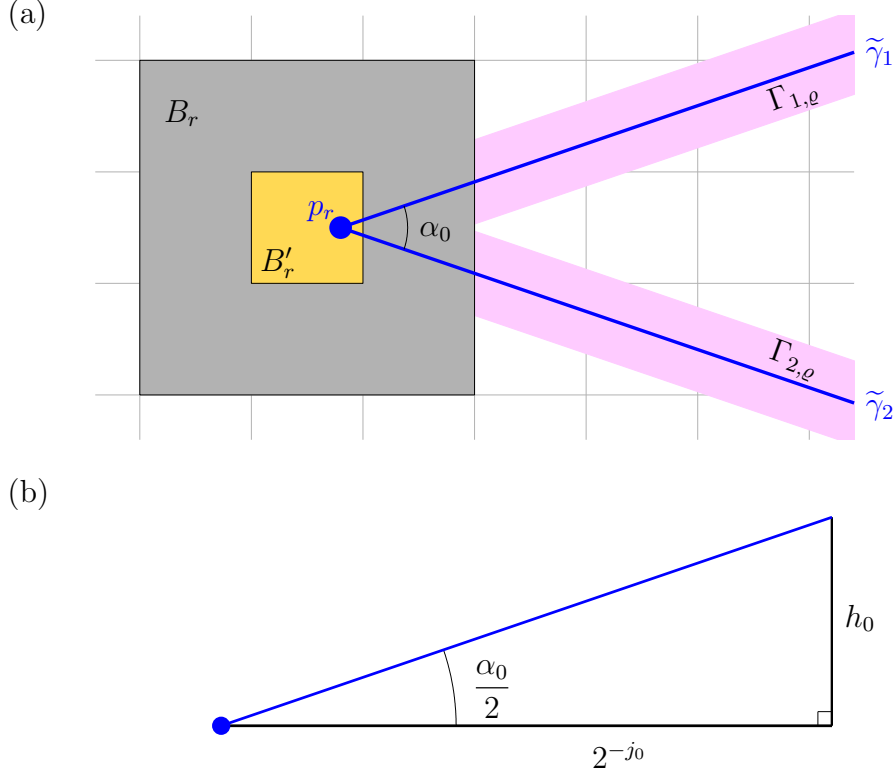


FIGURE 4. (a) Illustration of two disjoint sets $\Gamma_{1,\ell}$ and $\Gamma_{2,\ell}$ (pink) as defined in (2.14). The two edges $\tilde{\gamma}_1$ and $\tilde{\gamma}_2$, shown in blue, have the minimal angle α_0 between them. The construction of B_r and B'_r is done in the square grid of size $2^{-j_0} \times 2^{-j_0}$. (b) The worst-case limit situation when p_r is at the boundary of B'_r is where the definition (2.15) comes from.

See Figure 6 for illustration. Construct c_ℓ corresponding to each γ_ℓ with $\ell = 1, \dots, L$.

We move on to approximating functions using a square grid. Consider the function v_1 , which is piecewise constant in the triangulation of D , restricted to a tubular neighborhood $\Gamma_{\ell,\ell}$. The line segment $\tilde{\gamma}_\ell$ divides $\Gamma_{\ell,\ell}$ into two components, and v_1 has a constant value in each component. See Figure 7(b).

Now define another function v_2 , which is piecewise constant on the square grid of size $2^{-j_1} \times 2^{-j_1}$. Outside the tubular neighborhoods $\Gamma_{\ell,\ell}$ we set $v_1 \equiv v_2$. Inside $\Gamma_{\ell,\ell}$ we define the values of v_2 uniquely as follows. Consider the dyadic polygonal chains c_ℓ that are located close to the edges $\tilde{\gamma}_\ell$. Now v_2 is allowed to have discontinuities only along the curves c_ℓ or at the cluster boundaries ∂B_r . See Figure 7(c).

By the construction of the dyadic polygonal chains the area between an edge $\tilde{\gamma}_\ell$ and the polygonal chain is bounded by $3G2^{-j_1}$. Therefore we can estimate

$$(2.18) \quad \|v_1 - v_2\|_{L^1(D)} \leq 6MG2^{-j_1},$$

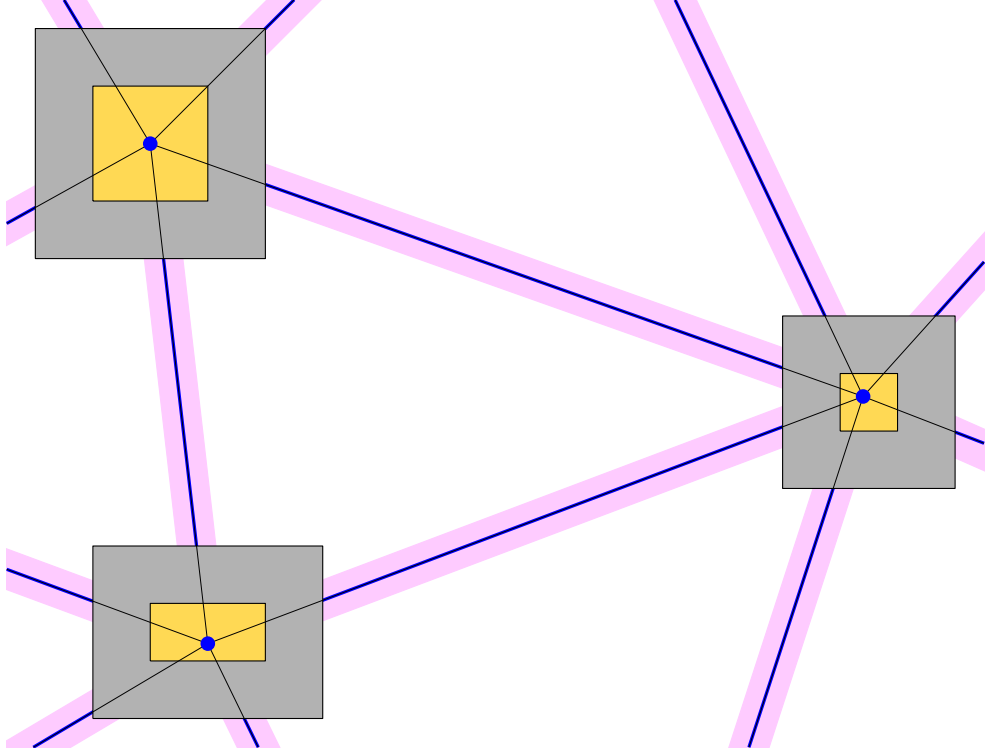


FIGURE 5. This is an illustration of the tubular neighborhoods $\Gamma_{\ell,\varrho}$ (pink), defined in (2.14), which are disjoint whenever $0 < \varrho < h_0$ with h_0 given by (2.15). The vertices p_r are shown as blue dots and the “triangle edges outside clusters,” or line segments $\tilde{\gamma}_\ell$ defined in (2.13), shown as blue lines.

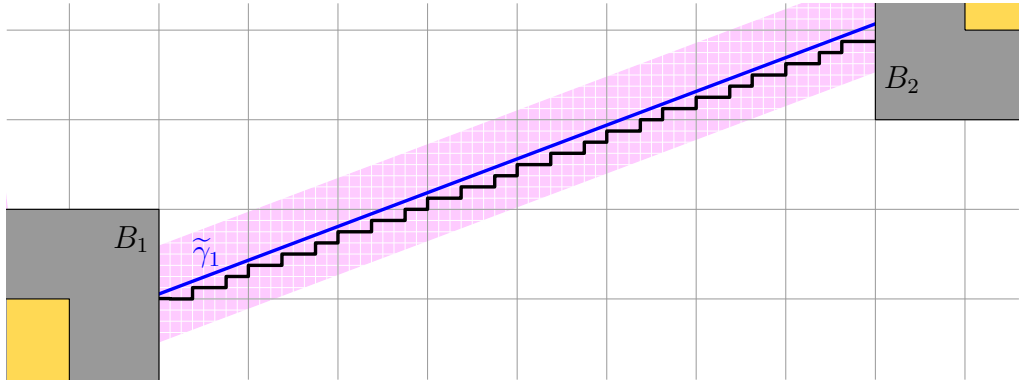


FIGURE 6. Refining the grid outside clusters. The bigger squares have size $2^{-j_0} \times 2^{-j_0}$ and the smaller squares have size $2^{-j_1} \times 2^{-j_1}$. A dyadic polygonal chain inside the tubular neighborhood $\Gamma_{1,\varrho}$ connects the clusters B_1 and B_2 .

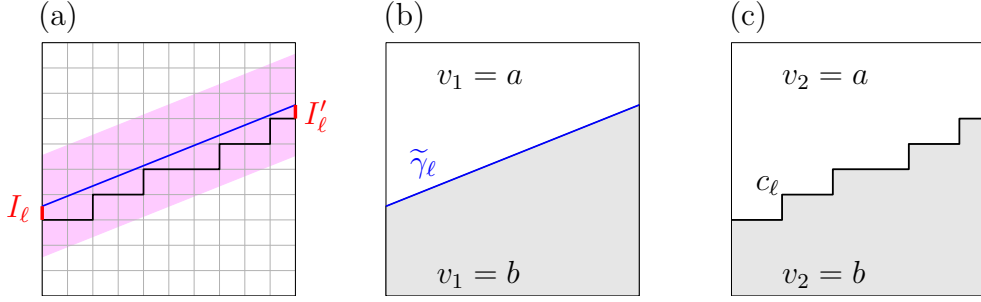


FIGURE 7. Square-grid based approximation of functions that are piecewise constant on a triangulation. (a) Detail from a situation similar to that shown in Figure 6. The straight blue line is the edge $\tilde{\gamma}_\ell$, and the black jagged line is the dyadic polygonal chain c_ℓ . The red intervals I_ℓ and I'_ℓ are used for estimating the difference between the BV norms of v_1 and v_2 . (b) A function v_1 which is piecewise constant on a triangulation. (c) Approximation of v_1 by another function v_2 which is piecewise constant on a square grid. The difference of the BV norms of v_1 and v_2 comes entirely from jumps over the two red vertical intervals shown in (a).

since we have $|v_1(x) - v_2(x)| \leq 2M$ for almost all $x \in D$.

Now both v_1 and v_2 are piecewise constant, and the domains of constant value are polygons. The expressions $V(v_1)$ and $V(v_2)$ can thus be calculated by summing the following quantities over the linear boundary segments: the jump in function values over the segment multiplied by the *Manhattan length of the segment*. Note that in $|V(v_1) - V(v_2)|$ all of the terms cancel each other except those coming from boundary segments located in the tubular neighborhoods $\Gamma_{\ell, \varrho}$. Due to the construction of c_ℓ , the Manhattan and Euclidean lengths of c_ℓ are the same. Further, the Manhattan length of $\tilde{\gamma}_\ell$ equals the length of c_ℓ , apart from the difference between the two red intervals I_ℓ and I'_ℓ shown in Figure 7(a). By (2.17) we have

$$||I_\ell| - |I'_\ell|| \leq |I_\ell| + |I'_\ell| \leq 6 \cdot 2^{-j_1}.$$

This together with the maximal jump size $2M$ allows us to estimate

$$(2.19) \quad |V(v_1) - V(v_2)| \leq 12ML2^{-j_1}.$$

Using (2.18) and (2.19) we see that for large enough j_1 we have $\rho_{1,1}(v_1, v_2) \leq \varepsilon/3$, and the proof is complete. \blacksquare

3. MULTI-RESOLUTION CONVERGENCE ANALYSIS

Define a functional $S_\infty : BV(D) \rightarrow \mathbb{R}$ by

$$(3.1) \quad S_\infty(u) = \|\mathcal{A}u - m\|_{L^2(\Omega)}^2 + \alpha_1 \|u\|_{L^1(D)} + \alpha V(u)$$

with positive regularization parameters $\alpha_1 > 0$ and $\alpha > 0$, and V given by (2.1). The functional S_∞ defines an infinite-dimensional minimization problem which we will approximate by discrete minimization problems. For this we define functionals $S_j : BV(D) \rightarrow \mathbb{R} \cup \{\infty\}$ by

$$(3.2) \quad S_j(u) = \begin{cases} S_\infty(u), & \text{for } u \in \text{Range}(T_j), \\ \infty, & \text{for } u \notin \text{Range}(T_j). \end{cases}$$

Denote

$$(3.3) \quad s_\infty := \inf_{u \in BV} S_\infty(u), \quad s_j := \inf_{u \in BV} S_j(u).$$

We study the existence and properties of minimizers $\tilde{u}_j, \tilde{u}_\infty \in BV(D)$ satisfying $S_j(\tilde{u}_j) = s_j$ and $S_\infty(\tilde{u}_\infty) = s_\infty$, respectively. Such minimizers may not be unique. Therefore, we use the notations

$$\begin{aligned} \arg \min(S_j) &= \{u \in BV(D) : S_j(u) = s_j\}, \\ \arg \min(S_\infty) &= \{u \in BV(D) : S_\infty(u) = s_\infty\}. \end{aligned}$$

We are now ready to state our main theorem.

Theorem 3.1. *Assume either (A) or (B) about the linear operator \mathcal{A} :*

- (A) $\mathcal{A} : L^2(D) \rightarrow L^2(\Omega)$ is compact and $\mathcal{A} : L^1(D) \rightarrow \mathcal{D}'(\Omega)$ is continuous with some open and bounded set $\Omega \subset \mathbb{R}^2$,
- (B) $\mathcal{A} : L^1(D) \rightarrow \mathbb{R}^M$ is bounded.

Let the functionals S_j and S_∞ be given by (3.2) and (3.1), respectively, and define s_j and s_∞ as in (3.3). Then

- (i) $\lim_{j \rightarrow \infty} s_j = s_\infty$.
- (ii) *There exists a minimizer $\tilde{u}_j \in \arg \min(S_j)$ for all $j = 1, 2, 3, \dots$*
- (iii) *There exists a minimizer $\tilde{u}_\infty \in \arg \min(S_\infty)$.*
- (iv) *Any sequence $\tilde{u}_j \in \arg \min(S_j)$ of minimizers has a subsequence $\tilde{u}_{j(\ell)}$ that converges weakly in $BV(D)$ to some limit $w \in BV(D)$, or more briefly $\tilde{u}_{j(\ell)} \xrightarrow{BVw} w$ as $\ell \rightarrow \infty$. Furthermore, $\lim_{\ell \rightarrow \infty} V(\tilde{u}_{j(\ell)}) = V(w)$, that is, the subsequence $\tilde{u}_{j(\ell)}$ converges to w in the intermediate topology of $BV(D)$.*
- (v) *The limit $w =: \tilde{u}_\infty$ in (iv) is a minimizer: $\tilde{u}_\infty \in \arg \min(S_\infty)$.*

The set Ω in (3.1) can be an open rectangle with $L^2(\Omega)$, modeling sinogram space, or $\Omega = \{1, 2, \dots, M\}$ equipped with the counting measure, leading to $L^2(\Omega) = \mathbb{R}^M$. These two options correspond to assumptions (A) and (B) in Theorem 3.1.

The connection between Theorem 3.1 and the computational explanation in the Introduction is this. In the computational part of this paper we take $\alpha_1 = 0$, which roughly corresponds to having a really small $\alpha_1 > 0$ in the theory. The minimizing

vector $\widehat{\mathbf{f}}_{\alpha,n} \in \mathbb{R}^{n \times n}$ defined in (1.3) can be seen as an $n \times n$ matrix with $n = 2^j$. The matrix $\widehat{\mathbf{f}}_{\alpha,n}$ is a 2D array of the values of a piecewise constant minimizer function $\tilde{u}_j \in \arg \min(S_j)$ in the pixels (2.6). Thus we see that for any choice of regularization parameter α in (1.3), the total variation norms of $\widehat{\mathbf{f}}_{\alpha,n}$ with $n = 2^j$ converge to a limit as $j \rightarrow \infty$. The measurement operator discussed in the Introduction is as in assumption (B).

Remark: our convergence result is quite delicate. Even a slight change of norms will destroy the argumentation. See Appendix B for more details about this.

Before proving the main theorem we prove a couple of lemmata.

Lemma 3.2. *Let the assumptions of Theorem 3.1 hold. Assume that $u_j \rightarrow u$ as $j \rightarrow \infty$ in the weak topology of $BV(D)$ given in Definition 2.2. Then*

$$(3.4) \quad \lim_{j \rightarrow \infty} \mathcal{A}u_j = \mathcal{A}u$$

with convergence in $L^2(\Omega)$ or in \mathbb{R}^M in the cases of Assumption (A) or (B) in Theorem 3.1, respectively. Moreover, it follows that

$$(3.5) \quad \begin{aligned} & \|\mathcal{A}u - m\|_{L^2(\Omega)}^2 + \alpha_1 \|u\|_{L^1(D)} + \alpha V(u) \\ & \leq \liminf_{j \rightarrow \infty} \left(\|\mathcal{A}u_j - m\|_{L^2(\Omega)}^2 + \alpha_1 \|u_j\|_{L^1(D)} + \alpha V(u_j) \right). \end{aligned}$$

Proof. Assume (A) of Theorem 3.1. By [1, Thm. 10.1.3] we have

$$\|u\|_{L^2(D)} \leq C_1 \|u\|_{BV(D)}.$$

Moreover, there is c_1 such that $\|u_j\|_{BV(D)} \leq c_1$ for all n . Hence, $\|u_j\|_{L^2(D)} \leq C$ for all j . To show that $\mathcal{A}u_j$ converges in $L^2(\Omega)$ to $\mathcal{A}u$ as $j \rightarrow \infty$, assume the opposite. Then there is $\varepsilon > 0$ and a subsequence $j(\ell) \rightarrow \infty$ as $\ell \rightarrow \infty$ such that

$$(3.6) \quad \|\mathcal{A}u_{j(\ell)} - \mathcal{A}u\|_{L^2(\Omega)} \geq \varepsilon.$$

Now $\|u_{j(\ell)}\|_{L^2(D)} \leq C$ and as $\mathcal{A} : L^2(D) \rightarrow L^2(\Omega)$ is compact, there is a subsequence $u_{j(\ell_p)}$ and $w \in L^2(\Omega)$ such that

$$(3.7) \quad \lim_{p \rightarrow \infty} \|\mathcal{A}u_{j(\ell_p)} - w\|_{L^2(\Omega)} = 0.$$

On the other hand, as $u_j \xrightarrow{BV_w} u$, we have that $u_j \rightarrow u$ in the strong topology of $L^1(D)$ by definition. This implies that

$$(3.8) \quad \lim_{p \rightarrow \infty} \mathcal{A}u_{j(\ell_p)} = \mathcal{A}u, \quad \text{in } \mathcal{D}'(\Omega).$$

The above two limits (3.7) in $L^2(\Omega)$ and (3.8) in $\mathcal{D}'(\Omega)$ imply that $\mathcal{A}u = w$. This, (3.6), and (3.7) are in contradiction. Hence we have (3.4) in the case of assumption (A) in Theorem 3.1.

Inequality (3.5) follows from the above and [1, Prop. 10.1.1].

Assumption (B) can be handled by adding a projection operator similar to (2.7). ■

Lemma 3.3. *Let the assumptions of Theorem 3.1 hold. Consider the functionals $S_j : (BV(D), \mathcal{T}'') \rightarrow [0, +\infty]$ defined in (3.2) and $S_\infty : (BV(D), \mathcal{T}'') \rightarrow [0, +\infty]$ defined in (3.1). Here \mathcal{T}'' denotes the intermediate topology of Definition 2.3.*

Then the sequence S_j of functionals Γ -converges to S_∞ as $j \rightarrow \infty$.

Proof. Note that one can use the distance function

$$d''(u_1, u_2) := \|u_1 - u_2\|_{L^1(D)} + \left| \int_D |\nabla u_1| dx - \int_D |\nabla u_2| dx \right|$$

to show that \mathcal{T}'' is metrizable. Because of the metrizability, showing Γ -convergence can be done by proving two things [13, Proposition 8.1]. The *lower-bound inequality*

$$(3.9) \quad S_\infty(u) \leq \liminf_{j \rightarrow \infty} S_j(u_j)$$

should hold whenever there is intermediate convergence of $u_j \in BV(D)$ to the limit $u \in BV(D)$. Further, we must show that for every $u \in BV(D)$ there is a sequence $u_j \in BV(D)$ converging intermediately to u and satisfying the *upper-bound inequality*

$$(3.10) \quad S_\infty(u) \geq \limsup_{j \rightarrow \infty} S_j(u_j).$$

Proving the upper-bound inequality (3.10). Take any $u \in BV(D)$. Recall the orthogonal projection operators $T_j : L^2(D) \rightarrow L^2(D)$ defined in (2.7), and the spaces $Y_j = \text{Range}(T_j)$ of piecewise constant functions. As $Y_j \subset Y_{j+1}$, by Lemma 2.4 there are $v_j \in Y_j$ such that $\lim_{j \rightarrow \infty} \rho_{1,1}(v_j, u) = 0$. This implies the following:

$$(3.11) \quad \lim_{j \rightarrow \infty} \|v_j - u\|_{L^1(D)} = 0,$$

$$(3.12) \quad \lim_{j \rightarrow \infty} V(v_j) = V(u),$$

$$(3.13) \quad V(v_j) \leq C_0 \text{ for all } j = 1, 2, 3, \dots, \text{ and for some } C_0 < \infty.$$

We claim that there is intermediate convergence of a subsequence of v_j to the limit u . The condition (2.4) was already established in (3.11). Regarding the condition (2.5), note that by (3.13) the total variation of v_j is bounded: $|\nabla v_j| \leq C_0$, and we can view the measures $|\nabla v_j|$ as a bounded sequence in the dual space $(C(D))^*$. Thus, by the Banach-Alaoglu theorem, there is a convergent subsequence $\nabla u_{j(\ell)}$ with $\ell = 1, 2, 3, \dots$, so that $\lim_{\ell \rightarrow \infty} \nabla u_{j(\ell)} = \eta \in (C(D))^*$. Now since v_j tends to u in $L^1(D)$ as $j \rightarrow \infty$, we have that $\nabla u_{j(\ell)}$ tends to ∇u in the sense of distributions as $\ell \rightarrow \infty$. Therefore, we must have $\eta = \nabla u$, and we have established intermediate convergence of $u_{j(\ell)}$ to u as $\ell \rightarrow \infty$.

Since $Y_j \subset Y_{j+1}$, we can construct a sequence $u_j \in Y_j$ for $j = 1, 2, 3, \dots$, by setting $u_m = v_{j(\ell)}$ for all $j(\ell) \leq m < j(\ell+1)$. Now there is intermediate convergence of u_j to u as $j \rightarrow \infty$. Thus we have $\lim_{j \rightarrow \infty} \|u_j\|_{L^1(D)} = \|u\|_{L^1(D)}$ and $\lim_{j \rightarrow \infty} V(u_j) = V(u)$. Furthermore, since intermediate convergence implies weak convergence, Lemma 3.2 shows that $\lim_{j \rightarrow \infty} \mathcal{A}u_j = \mathcal{A}u$ in $L^2(\Omega)$. Now the fact that $u_j \in Y_j$ and formula

(3.2) together imply $S_j(u_j) = S_\infty(u_j)$. Therefore the upper-bound inequality (3.10) follows from

$$\begin{aligned} & \|\mathcal{A}u - m\|_{L^2(\Omega)}^2 + \alpha_1 \|u\|_{L^1(D)} + \alpha V(u) \\ &= \lim_{j \rightarrow \infty} \left(\|\mathcal{A}u_j - m\|_{L^2(\Omega)}^2 + \alpha_1 \|u_j\|_{L^1(D)} + \alpha V(u_j) \right). \end{aligned}$$

Proving the lower-bound inequality (3.9). Assume that u_j converges intermediately to u in BV as $j \rightarrow \infty$. Then by definition we have $\lim_{j \rightarrow \infty} \|u_j\|_{L^1(D)} = \|u\|_{L^1(D)}$, and (3.4) shows that $\lim_{j \rightarrow \infty} \|\mathcal{A}u_j - m\|_{L^2(\Omega)} = \|\mathcal{A}u - m\|_{L^2(\Omega)}$. Moreover, intermediate convergence implies $V(u) \leq \liminf_{j \rightarrow \infty} V(u_j)$, see [1, Proposition 10.1.2]. Now estimate

$$\begin{aligned} S_\infty(u) &= \|\mathcal{A}u - m\|_{L^2(\Omega)}^2 + \alpha_1 \|u\|_{L^1(D)} + \alpha V(u) \\ &\leq \lim_{j \rightarrow \infty} \|\mathcal{A}u_j - m\|_{L^2(\Omega)}^2 + \alpha_1 \lim_{j \rightarrow \infty} \|u_j\|_{L^1(D)} + \alpha \liminf_{j \rightarrow \infty} V(u_j) \\ &= \liminf_{j \rightarrow \infty} \|\mathcal{A}u_j - m\|_{L^2(\Omega)}^2 + \alpha_1 \liminf_{j \rightarrow \infty} \|u_j\|_{L^1(D)} + \alpha \liminf_{j \rightarrow \infty} V(u_j) \\ &\leq \liminf_{j \rightarrow \infty} \left(\|\mathcal{A}u_j - m\|_{L^2(\Omega)}^2 + \alpha_1 \|u_j\|_{L^1(D)} + \alpha V(u_j) \right) \\ &= \liminf_{j \rightarrow \infty} S_\infty(u_j) \\ (3.14) \quad &\leq \liminf_{j \rightarrow \infty} S_j(u_j). \end{aligned}$$

■

Proof of Theorem 3.1. Let us restrict S_j and S_∞ to the set

$$\mathcal{B}_R = \{u \in BV(D) : (\alpha_1 \|u\|_{L^1(D)} + \alpha V(u)) \leq R\}$$

and call the resulting functionals $S_j^{(R)}$ and $S_\infty^{(R)}$, respectively. Denote by \mathcal{T}' the topology in $\mathcal{B}_R \subset BV(D)$ induced by the weak topology of $BV(D)$. Since $C(D)$ is separable, the space $(\mathcal{B}_R, \mathcal{T}')$ is metrizable and, in particular, satisfies the 1st axiom of countability as a topological space.

Next we show that the restricted functionals $S_j^{(R)}$ Γ -converge to the restricted limit functional $S_\infty^{(R)}$. When $u_j \in \mathcal{B}_R$ converges in the weak topology to the limit $u \in \mathcal{B}_R$, the lower-bound inequality (3.9) follows from Lemma 3.2. Furthermore, Lemma 3.3 yields that for all $u \in \mathcal{B}_R$ there is some sequence u_j converging to u in the intermediate topology of BV for which the upper-bound inequality (3.10) holds. Then, we see that the sequence

$$(3.15) \quad v_j(x) := \frac{V(u) + \|u\|_{L^1(D)}}{V(u_j) + \|u_j\|_{L^1(D)} + \frac{1}{j}} u_j(x)$$

satisfies $v_j \in \mathcal{B}_R$, v_j converges to u in the intermediate topology of BV , and that the upper-bound inequality (3.10) is valid also for the sequence v_j and u . As the intermediate convergence in BV implies the weak convergence in BV , these facts

show that $S_j^{(R)}$ Γ -converge to $S_\infty^{(R)}$, in $(\mathcal{B}_R, \mathcal{T}')$, as $j \rightarrow \infty$ for any fixed $R > 0$, see e.g. [2, 1].

Let us prove the existence of minimizers for $S_\infty^{(R)}$ and $S_j^{(R)}$. Note first that

- by Lemma 3.2 the functionals S_∞ and S_j are lower semicontinuous with respect to the weak topology of $BV(D)$, and
- by the Banach-Alaoglu theorem and [1, Theorem 10.1.4] the space $(\mathcal{B}_R, \mathcal{T}')$ is compact.

Therefore, the functionals S_∞ and S_j have minimizers for any $R > 0$.

Set $R = s_\infty + 1$ with s_∞ defined in (3.3). Then there exists a minimizer $\tilde{u}_\infty \in \operatorname{argmin}(S_\infty^{(R)})$ belonging to the open interior of \mathcal{B}_R .

Using (3.15) we see that there are $u_j \in Y_j \cap \mathcal{B}_R$ for which $u_j \rightarrow \tilde{u}_\infty$ in the intermediate topology and (3.14) holds. For all large enough j we have

$$S_\infty(u_j) \leq S_\infty(\tilde{u}_\infty) + 1 = s_\infty + 1.$$

As $S_j(u_j) = S_\infty(u_j)$ and $S_m(u) \leq S_j(u)$ for $m \geq j$, we see that for all large enough j the minimizers of the functionals $S_j^{(R)}$ coincide with the minimizers of S_j . Therefore we do not lose any generality in our minimization analysis by restricting to \mathcal{B}_R .

Let us now study the convergence properties of minimizers. As we saw above, for large enough j all minimizers $\tilde{u}_j \in \operatorname{argmin}(S_j) = \operatorname{argmin}(S_j^{(R)})$ and $\tilde{u}_\infty \in \operatorname{argmin}(S_\infty) = \operatorname{argmin}(S_\infty^{(R)})$ are in the ball \mathcal{B}_R . The compactness of $(\mathcal{B}_R, \mathcal{T}')$ implies that any sequence $(\tilde{u}_j)_{j=1}^\infty$ of minimizers has a subsequence $(\tilde{u}_{j(\ell)})_{\ell=1}^\infty$ converging to some $w \in \mathcal{B}_R$ in the weak topology of BV . By [13, Cor. 7.20], the limit w is then a minimizer of $S_\infty^{(R)}$ and we have

$$(3.16) \quad \lim_{\ell \rightarrow \infty} S_{j(\ell)}(\tilde{u}_{j(\ell)}) = \lim_{\ell \rightarrow \infty} S_{j(\ell)}^{(R)}(\tilde{u}_{j(\ell)}) = S_\infty^{(R)}(w) = S_\infty(w) = s_\infty.$$

Moreover, by [13, Cor. 7.20], the equation (3.16) holds for an arbitrary sequence $u_{j(\ell)} \in \operatorname{argmin}(S_{j(\ell)})$, $\ell = 1, 2, \dots$ that converge in the weak topology of BV to some limit w , and w is a minimizer of S_∞ .

Let us next consider a subsequence $\tilde{u}_{j(\ell)} \in \operatorname{argmin}(S_{j(\ell)})$ converging to $\tilde{u}_\infty \in \operatorname{argmin}(S_\infty)$ in the weak topology of BV . Then we have

$$(3.17) \quad V(\tilde{u}_\infty) \leq \liminf_{\ell \rightarrow \infty} V(\tilde{u}_{j(\ell)}).$$

Assume that we would have here a strict inequality.

By definition we have for any subsequence $\tilde{u}_{j(\ell)}$ converging to \tilde{u}_∞ in the weak topology of BV

$$\|\tilde{u}_\infty\|_{L^1(D)} = \lim_{\ell \rightarrow \infty} \|\tilde{u}_{j(\ell)}\|_{L^1(D)}.$$

By Lemma 3.2, we have

$$(3.18) \quad \|\mathcal{A}\tilde{u}_\infty - m\|_{L^2(\Omega)}^2 = \lim_{\ell \rightarrow \infty} \|\mathcal{A}\tilde{u}_{j(\ell)} - m\|_{L^2(\Omega)}^2.$$

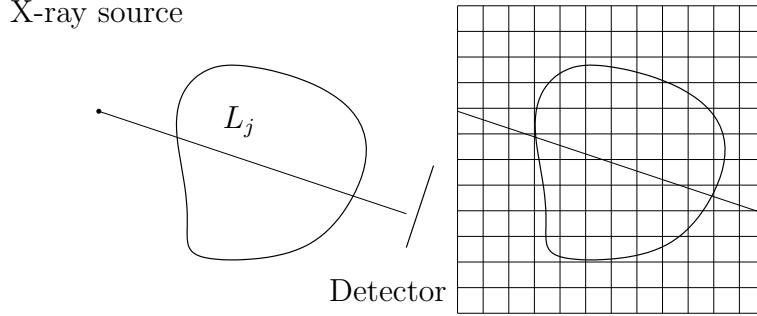


FIGURE 8. Left: Illustration of the pencil-beam attenuation model of X-ray tomography. Right: Domain Ω discretized into a lattice of pixels/voxels Ω_i

These and a strict inequality in (3.17) would imply that $\liminf_{\ell \rightarrow \infty} S_{j(\ell)}(u_{j(\ell)}) < s_\infty$, but that is not possible in view of (3.16). Therefore,

$$(3.19) \quad V(\tilde{u}_\infty) = \liminf_{\ell \rightarrow \infty} V(\tilde{u}_{j(\ell)}).$$

Similar arguments with \liminf replaced by \limsup yield the desired equality. ■

4. COMPUTATIONAL MODELS AND ALGORITHMS

4.1. X-ray attenuation model. In X-ray imaging the radiation source is placed on one side of an object and the detector at the opposite side. The rays pass through the object and the attenuated signal is detected by a digital sensor (array of almost point-like detectors), see Figure 8 for an illustration. We model the (2D slice of the) object by a rectangle $\Omega \subset \mathbb{R}^2$ and by a non-negative attenuation coefficient $u : \Omega \rightarrow [0, \infty)$. The attenuation coefficient u gives the relative intensity loss of an X-ray travelling a small distance ds at $s \in \Omega$. This leads to the following linear model

$$(4.1) \quad g_j = -\log \left(\frac{I_j}{I_0} \right) = \int_{L_j} u(s) ds,$$

where L_j is the j th line of the X-ray, g_j is the value of the projection measurement of the j th source to detector line L_j , I_j is the measured X-ray intensity and I_0 is the initial intensity of the X-ray beam before entering Ω .

We discretize this model by dividing the domain Ω into a lattice of pixels Ω_i and by computing the length of the path L_j inside each pixel Ω_i , see figure 8. Assuming that the attenuation function $u(s)$ is constant inside each pixel Ω_i , the projection

measurements g_j can be approximated by

$$(4.2) \quad g_j = \int_{L_j} u(s) ds \approx \sum_i f_i |\Omega_i \cap L_j|,$$

where f_i is the constant value of the function u in the i th pixel and $|\Omega_i \cap L_j|$ denotes the length of the ray L_j through pixel Ω_i . Arranging the set of M measurements into a vector $\mathbf{g} = (g_1, g_2, \dots, g_M) \in \mathbb{R}^M$, we obtain the model

$$\mathbf{g} = A\mathbf{f},$$

where $\mathbf{f} \in \mathbb{R}^N = \mathbb{R}^{n \times n}$ is the vector containing the attenuation values in the pixels and $A \in \mathbb{R}^{M \times N}$ is the matrix that implements the transform from the pixel values to the projection data, see equation (4.2).

4.2. Discrete anisotropic TV. We consider the anisotropic total variation

$$\|\mathbf{f}\|_{\text{TV}} = \|D_H \mathbf{f}\|_1 + \|D_V \mathbf{f}\|_1$$

where the $N \times N$ matrices D_H and D_V implement horizontal and vertical differences in the $n \times n$ pixel image represented by vector \mathbf{f} . We use periodic boundary conditions. See Appendix A for an example of the construction of D_H and D_V .

Now the TV regularized X-ray imaging problem (1.3) can be rewritten as follows:

$$(4.3) \quad \arg \min_{\mathbf{f} \in \mathbb{R}_+^N} \left\{ \frac{1}{2} \|A\mathbf{f} - \tilde{\mathbf{g}}\|_2^2 + \alpha (\|D_H \mathbf{f}\|_1 + \|D_V \mathbf{f}\|_1) \right\}.$$

4.3. Quadratic programming. The minimization problem of (4.3) can be reformulated as a quadratic programming problem. Denoting $D_H \mathbf{f} = \mathbf{h}^+ - \mathbf{h}^-$ and $D_V \mathbf{f} = \mathbf{v}^+ - \mathbf{v}^-$ (4.3) can be rewritten as follows

$$\arg \min \left\{ \frac{1}{2} \mathbf{f}^T A^T A \mathbf{f} - \mathbf{f}^T A^T \tilde{\mathbf{g}} + \alpha \mathbf{1}^T \mathbf{h}^+ + \alpha \mathbf{1}^T \mathbf{h}^- + \alpha \mathbf{1}^T \mathbf{v}^+ + \alpha \mathbf{1}^T \mathbf{v}^- + \frac{1}{2} \tilde{\mathbf{g}}^T \tilde{\mathbf{g}} \right\},$$

where $\mathbf{1}$ is a vector of all ones and $\mathbf{h}^+, \mathbf{h}^-, \mathbf{v}^+, \mathbf{v}^- \geq 0$. Further we can denote

$$\mathbf{z} = \begin{bmatrix} \mathbf{f} \\ \mathbf{h}^+ \\ \mathbf{h}^- \\ \mathbf{v}^+ \\ \mathbf{v}^- \end{bmatrix}, \quad Q = \begin{bmatrix} A^T A & 0 & 0 & 0 & 0 \\ 0 & 0 & 0 & 0 & 0 \\ 0 & 0 & 0 & 0 & 0 \\ 0 & 0 & 0 & 0 & 0 \\ 0 & 0 & 0 & 0 & 0 \end{bmatrix}, \quad \mathbf{c} = \begin{bmatrix} -A^T \tilde{\mathbf{g}} \\ \alpha \mathbf{1} \\ \alpha \mathbf{1} \\ \alpha \mathbf{1} \\ \alpha \mathbf{1} \end{bmatrix}, \quad d = \frac{1}{2} \tilde{\mathbf{g}}^T \tilde{\mathbf{g}}.$$

Now we can write

$$(4.4) \quad \begin{aligned} \min_{\mathbf{z}} \quad & \frac{1}{2} \mathbf{z}^T Q \mathbf{z} + \mathbf{c}^T \mathbf{z} + d \\ \text{s.t.} \quad & \mathcal{B} \mathbf{z} = \mathbf{b} \\ & \mathbf{z} \geq 0 \end{aligned}$$

where Q is symmetric and positive definite matrix and

$$\mathcal{B} = \begin{bmatrix} D_H & -I & I & O & O \\ D_V & O & O & -I & I \end{bmatrix},$$

I denotes identity matrix and O denotes a matrix of all zeros.

4.4. Primal-dual interior-point (PD-IP) method. The formulation of the primal-dual interior-point algorithm starts by rewriting the primal problem (4.4) as a logarithmic barrier problem [20]

$$(4.5) \quad \begin{aligned} \min_{\mathbf{z}} \quad & \frac{1}{2} \mathbf{z}^T Q \mathbf{z} + \mathbf{c}^T \mathbf{z} + d - \mu \sum \log(\mathbf{z}) \\ \text{s.t} \quad & \mathcal{B} \mathbf{z} = \mathbf{b}. \end{aligned}$$

To solve this minimization problem, we introduce the Lagrangian function

$$(4.6) \quad \mathcal{L}(\mathbf{z}, \mathbf{y}; \mu) = \frac{1}{2} \mathbf{z}^T Q \mathbf{z} + \mathbf{c}^T \mathbf{z} + d - \mu \sum \log(\mathbf{z}) - \mathbf{y}^T (\mathcal{B} \mathbf{z} - \mathbf{b}),$$

where \mathbf{y} is the Lagrangian multiplier. We note that the Lagrangian multiplier \mathbf{y} is also the dual variable of the associated Lagrangian dual problem. For further information see [59, 46], for example.

Now the minimization problem of (4.5) can be solved by seeking a stationary point for the Lagrangian function. Differentiating the Lagrangian with respect to primal ($\mathbf{z} \in \mathbb{R}^{n_z}$) and dual ($\mathbf{y} \in \mathbb{R}^{n_y}$) variables yields

$$\begin{aligned} 0 = \nabla_{\mathbf{z}} \mathcal{L}(\mathbf{z}, \mathbf{y}; \mu) &= Q \mathbf{z} + \mathbf{c} - \mu Z^{-1} \mathbf{1} + \mathcal{B}^T \mathbf{y} \\ 0 = \nabla_{\mathbf{y}} \mathcal{L}(\mathbf{z}, \mathbf{y}; \mu) &= \mathbf{b} - \mathcal{B} \mathbf{z}. \end{aligned}$$

These conditions are the first order necessary optimality conditions, often referred to as the Karush-Kuhn-Tucker (KKT) conditions.

To derive the primal-dual (path-following) method we consider the perturbed KKT conditions [46, 59]. Denoting $\mu Z^{-1} \mathbf{1} = \tilde{\mathbf{x}}$, the perturbed KKT conditions can be written as a mapping $\mathcal{F} : \mathbb{R}^{2n_z+n_y} \rightarrow \mathbb{R}^{2n_z+n_y}$

$$(4.7) \quad \mathcal{F}(\mathbf{z}, \tilde{\mathbf{x}}, \mathbf{y}; \mu) = \begin{bmatrix} Q \mathbf{z} - \mathcal{B}^T \mathbf{y} - \tilde{\mathbf{x}} + \mathbf{c} \\ \mathcal{B} \mathbf{z} - \mathbf{b} \\ Z \tilde{X} \mathbf{1} - \mu \mathbf{1}, \end{bmatrix}$$

where $Z = \text{diag}(z_1, z_2, \dots, z_{n_z})$, $\tilde{X} = \text{diag}(\tilde{x}_1, \tilde{x}_2, \dots, \tilde{x}_{n_z})$ and $\mu > 0$ is the central path parameter. The central path is defined by the trajectory $\mathcal{P} : \mathcal{P}\{\mathbf{z}_\mu, \mathbf{y}_\mu, \tilde{\mathbf{x}}_\mu | \mu > 0\}$. As $\mu \rightarrow 0$ the trajectory \mathcal{P} converges to optimal solution of both the primal and dual problems. Note that at the optimal point $\mu = 0$.

Applying Newton's method to (4.7), we obtain a linear system of the form

$$(4.8) \quad \begin{bmatrix} -Q & \mathcal{B}^T & I \\ \mathcal{B} & 0 & 0 \\ I & 0 & \tilde{X}^{-1} Z \end{bmatrix} \begin{bmatrix} \Delta \mathbf{z} \\ \Delta \mathbf{y} \\ \Delta \tilde{\mathbf{x}} \end{bmatrix} = \begin{bmatrix} \mathbf{p}_1 \\ \mathbf{p}_2 \\ \mathbf{p}_3 \end{bmatrix},$$

where I is identity matrix, $\mathbf{p}_1 = \mathbf{c} + Q \mathbf{z} - \mathcal{B}^T \mathbf{y} - \tilde{\mathbf{x}}$, $\mathbf{p}_2 = \mathbf{b} - \mathcal{B} \mathbf{z}$ and $\mathbf{p}_3 = \mu / \tilde{\mathbf{x}} - \mathbf{z} - \Delta \tilde{\mathbf{x}} \Delta \mathbf{z} / \tilde{\mathbf{x}}$. The variable $\Delta \tilde{\mathbf{x}}$ can be removed without producing any off-diagonal entries in the remaining system. Hence the KKT conditions can be written

in a more compact way as

$$(4.9) \quad \begin{bmatrix} -(Q + Z^{-1}\tilde{X}) & \mathcal{B}^T \\ \mathcal{B} & 0 \end{bmatrix} \begin{bmatrix} \Delta \mathbf{z} \\ \Delta \mathbf{y} \end{bmatrix} = \begin{bmatrix} \mathbf{p}_1 - Z^{-1}\tilde{X}\mathbf{p}_3 \\ \mathbf{p}_2 \end{bmatrix},$$

with $\Delta \tilde{\mathbf{x}} = Z^{-1}\tilde{X}(\mathbf{p}_3 - \Delta \mathbf{z})$.

4.5. The PD-IP algorithm. The PD-IP method presented here is an iterative method and is based on Mehrotra's predictor-corrector approach [41]. The resulting algorithm can be summarized as follows.

Algorithm:

for $k = 0, 1, 2, \dots$

 Compute $(\mathbf{z}^0, \mathbf{y}^0, \tilde{\mathbf{x}}^0)$, with $\mathbf{z}^0, \tilde{\mathbf{x}}^0 > 0$

 Set $\mu = 0, \Delta \mathbf{z} = 0$ and $\Delta \tilde{\mathbf{x}} = 0$ and solve (4.9) to compute the predictor steps $(\Delta \mathbf{z}^{\text{pre}}, \Delta \mathbf{y}^{\text{pre}}, \Delta \tilde{\mathbf{x}}^{\text{pre}})$.

 Compute a value for μ .

 Compute \mathbf{p}_3 using $(\Delta \mathbf{z}^{\text{pre}}, \Delta \mathbf{y}^{\text{pre}}, \Delta \tilde{\mathbf{x}}^{\text{pre}})$ of step 2 and μ of step 3.

 Solve (4.9) for $(\Delta \mathbf{z}, \Delta \mathbf{y}, \Delta \tilde{\mathbf{x}})$.

 Compute step length multipliers λ_{primal} and λ_{dual}

 Set

$$\begin{aligned} \mathbf{z}^{k+1} &= \mathbf{z}^k + \lambda_{\text{primal}} \Delta \mathbf{z} \\ \mathbf{y}^{k+1} &= \mathbf{y}^k + \lambda_{\text{dual}} \Delta \mathbf{y} \\ \tilde{\mathbf{x}}^{k+1} &= \tilde{\mathbf{x}}^k + \lambda_{\text{dual}} \Delta \tilde{\mathbf{x}} \end{aligned}$$

end for

For further details of the algorithm see [45].

5. RESULTS

5.1. X-ray measurement data. The parameter selection method was tested using experimental X-ray tomography data from a walnut¹. The projection data of the walnut was acquired with a custom-built μ CT device nanotom 180 supplied by Phoenix Xray Systems + Services GmbH (Wunstorf, Germany). The measurement set-up is presented in figure 9. The chosen geometry resulted in a magnification with resolution of $18.33 \mu\text{m}/\text{pixel}$. The X-ray detector is a 12-bit CMOS flat panel detector with 2304×2284 pixels of $50 \mu\text{m}$ size (Hamamatsu Photonics, Japan). A set of 90 projection images were acquired over a 180 degree rotation with uniform angular step of 2 degrees between projections. Each projection image was composed of an average of six 750 ms exposures. The X-ray tube acceleration voltage was 80 kV and tube current $200 \mu\text{A}$, and the full polychromatic beam was used for image acquisition. For this work we chose only the projections corresponding to the middle cross-section of the walnut, thus resulting to a 2D reconstruction task.

We consider two test cases:

¹The data is made open access at: <http://www.fips.fi/dataset.php>

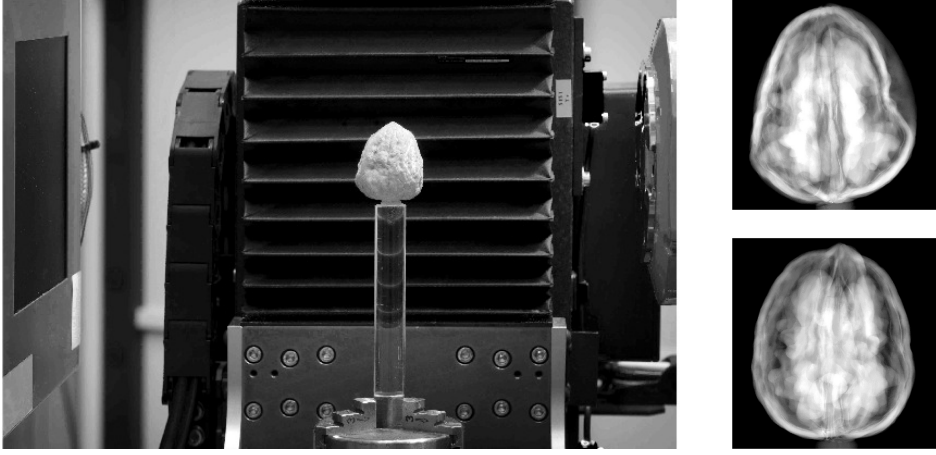


FIGURE 9. Left: Experimental setup for collecting tomographic X-ray data of a walnut. The detector plane is on the left and the X-ray source on the right in the picture. The walnut is attached to a computer-controlled rotator platform. Right: Two examples of the resulting projection images.

- i) Reconstruction using the measured X-ray data
- ii) Reconstruction using the measured X-ray data with 5% additional additive random noise, i.e., using measurement $\tilde{\mathbf{g}} + \mathbf{e}$ where \mathbf{e} is realization from multivariate Gaussian with standard deviation equivalent to 5% of the maximum value of the actual measurement $\tilde{\mathbf{g}}$.

5.2. Selection of α using the parameter choice rule. In this work we consider three levels of discretization: $n = 128, 192, 256$, each resulting to a 2D reconstruction on a $n \times n$ grid. TV regularized reconstructions $\hat{\mathbf{f}}_{\alpha,n}$ were computed with several values of regularization parameter α by solving the minimization problem of (4.3) using the algorithm of section 4.5.

Total variation norms $\|\hat{\mathbf{f}}_{\alpha,n}\|_{\text{TV}}$ of the reconstructed images were computed as a function of α at each discretization level n . Results from the measured data (case i) and from the measured data corrupted with 5% of random additional noise (case ii) are shown in Table 1. A few samples of the corresponding reconstructions are shown in figures 10 and 11 for test cases i) and ii), respectively.

The reconstructions in figures 10 and 11 are selected as follows. On the top row the value of the regularization parameter is too small producing a "noisy" reconstruction and on the bottom row the regularization parameter is too big producing an "over-regularized" reconstruction. In the middle row the value of the regularization parameter is selected as the smallest keeping the TV norms of reconstructions approximately independent of resolution. See Table 1.

TABLE 1. TV norms of 2D reconstructions $\hat{\mathbf{f}}_{\alpha,n}$ computed on three different discretization levels with several values of α ranging in the interval $[10^{-6}, 10^6]$. The discretization levels were set to $n = 128, 192, 256$. The results are computed from projection data with 90 projection angles. Data is corrupted with additional additive random noise (5%). Approximately resolution-independent TV norms are highlighted. The choice of α is the smallest possible leading to stable TV norms: $\alpha = 1$ in the case of low noise, and $\alpha = 10$ in the case of 5% added noise.

	Low noise			5% noise		
α	128^2	192^2	256^2	128^2	192^2	256^2
10^{-4}	1.51	2.29	3.64	2.42	5.05	8.71
10^{-3}	1.51	2.29	3.46	2.43	5.05	8.59
10^{-2}	1.50	2.23	2.97	2.42	5.01	8.59
10^{-1}	1.43	1.85	1.93	2.37	4.83	8.16
10^0	1.08	1.11	1.11	1.99	3.50	5.12
10^1	0.78	0.78	0.77	0.86	0.86	0.88
10^2	0.48	0.48	0.48	0.48	0.48	0.48
10^3	0.12	0.12	0.12	0.12	0.12	0.12
10^4	0.04	0.04	0.04	0.04	0.04	0.04
10^5	0	0	0	0	0	0
10^6	0	0	0	0	0	0

5.3. Selection of α using the S-curve method. The S-curve method was originally introduced in [35, 27] within a Bayesian inversion framework. In this work we apply the S-curve method for TV regularized tomography.

The S-curve was applied as follows. For test case i), we computed TV regularized reconstructions $\hat{\mathbf{f}}_{\alpha,n}$ with fixed n for 14 different values of α ranging in the interval $[10^{-6}, 10^6]$ and computed the TV norms

$$S(\alpha) := \|\hat{\mathbf{f}}_{\alpha,n}\|_{\text{TV}}$$

for the reconstructions. Then the data $\{\alpha, S(\alpha)\}$ was interpolated to get the S-curve. The S-curve was computed using the same three different discretization levels ($n = 128, 192, 256$) that were used in section 5.2.

In the test case ii) we computed reconstructions with 14 different values of α ranging in the interval $[10^{-4}, 10^8]$, and applied the S-curve interpolation procedure similarly as in case i).

As in [27] the *a priori* value for the sparsity level \hat{S} was estimated using three digital photographs of split walnuts. The photographs of the three walnuts are shown in figure 12. The walnut used to measure the X-ray data is not included in the photos. In reality, as is the case also in this work, the *a priori* information, that we use to estimate the value of \hat{S} , comes from a different modality (e.g. anatomical atlases) than the one we are considering (here digital photographs versus X-ray

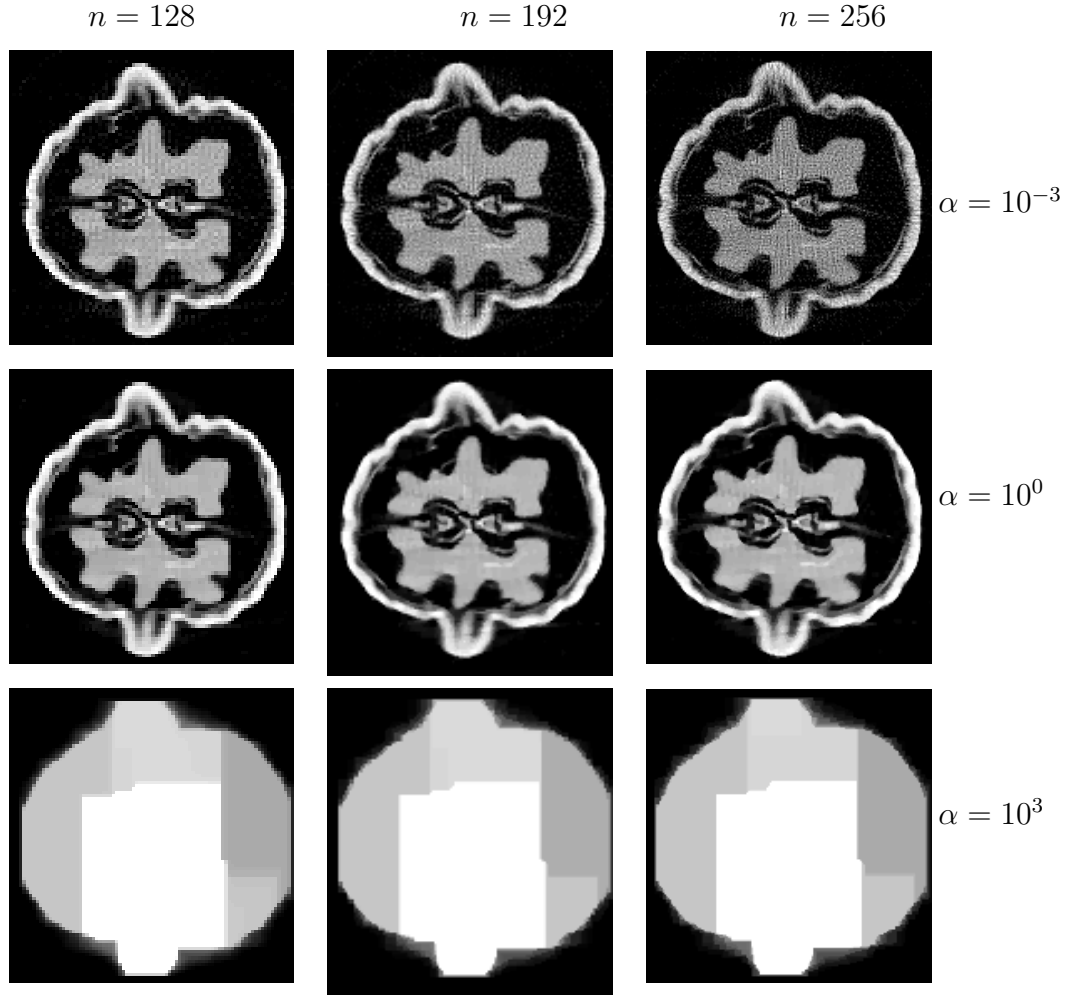


FIGURE 10. TV regularized reconstructions $\hat{\mathbf{f}}_{\alpha,n}$ from the projection data of the walnut computed with different values of regularization parameter α . The values of α are indicated on the right. Discretization levels $n = 128, 192, 256$ are indicated on the top.

attenuation function). Therefore in order to compute the \hat{S} for the total variation regularized X-ray tomography, each of the digital photographs \mathbf{f}_p were scaled such that the norm of the computed X-ray projection data of the photograph is the same as the norm of the measured projection data $\tilde{\mathbf{g}}$. This was obtained by

$$(5.1) \quad \tilde{\mathbf{f}}_p = \frac{\|\tilde{\mathbf{g}}\|}{\|A\mathbf{f}_p\|} \mathbf{f}_p$$

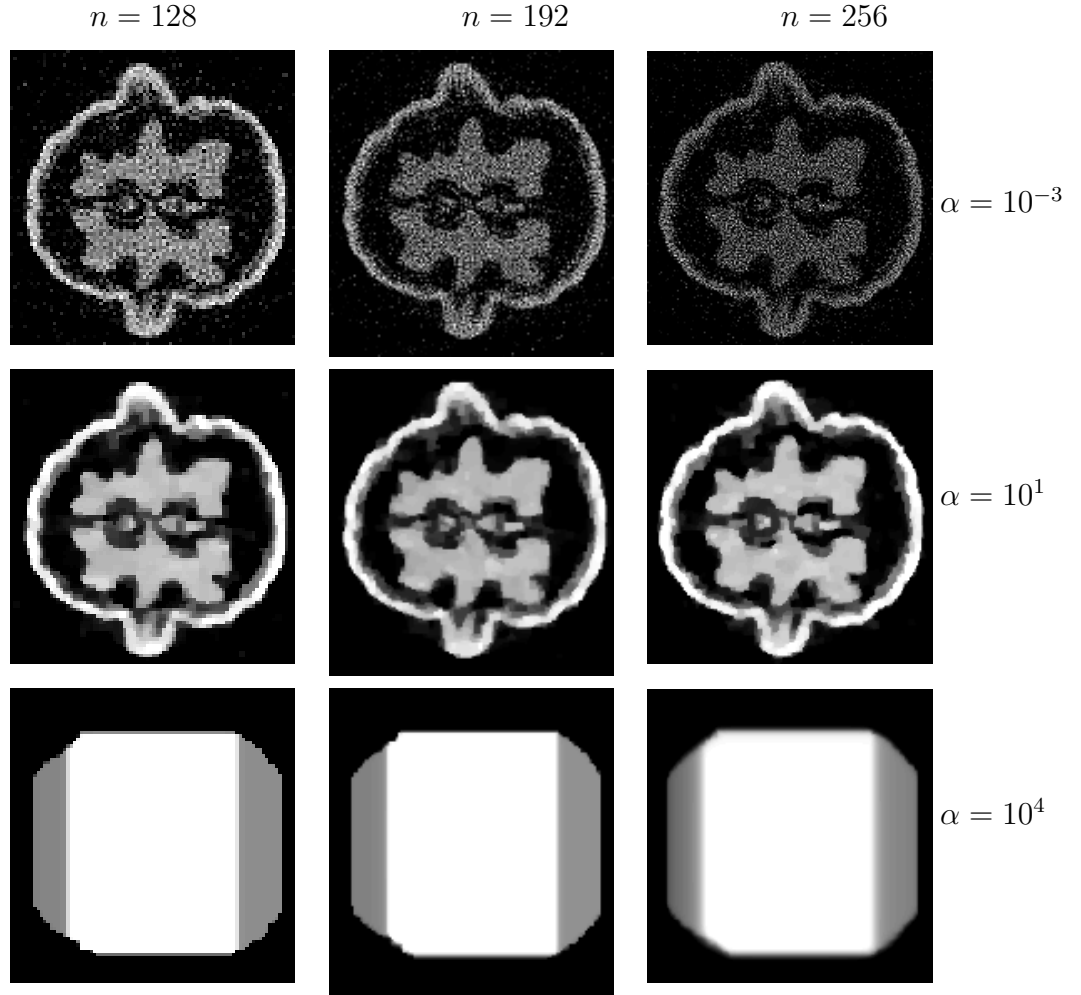


FIGURE 11. TV regularized reconstructions $\hat{\mathbf{f}}_{\alpha,n}$ from the measured projection data corrupted with 5% additional noise computed with different values of regularization parameter α . The values of α are denoted on the right. Discretization levels $n = 128, 192, 256$ are indicated on the top.

This scaling of the photographs is essential since the total variations of the photographs are not directly comparable to the total variation of the X-ray attenuation function.

The S-curve plots and the resulting reconstructions for each discretization levels are presented in figure 13. Corresponding results with 5 % additional noise are presented in figure 14.

As a reference, results with L-curve method were computed with both test cases i) and ii). The L-curve plots and corresponding reconstructions are here shown only

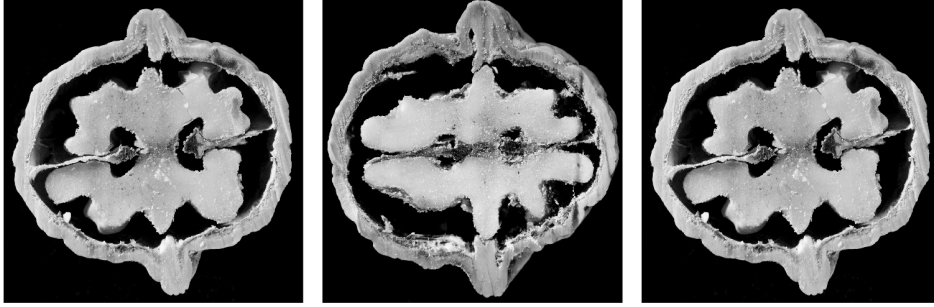


FIGURE 12. Photographs of three walnuts split in half. These images were used to provide *a priori* information about the expected total variation of the target. Of course, these are optical photographs and thus physically very different objects from the reconstructions (tomographic slices representing X-ray attenuation coefficient). However, we assume that the total variations of the photographs, when scaled by (5.1), are comparable to the total variation of the X-ray attenuation coefficient.

for the discretization level $n = 128$, but the results for other discretization levels were similar. Figures 15 and 16, present the L-curve plots and the corresponding reconstructions for the test cases i) and ii), respectively.

6. DISCUSSION AND CONCLUSIONS

The results listed in Table 1 provide numerical evidence supporting the proposed parameter choice rule. It seems that the new multiresolution-based parameter choice rule finds useful and robust values for the Total Variation regularization parameter without the need for any *a priori* information. The fact that we use measured X-ray projection data (as opposed to simulated data) lends credibility to these initial findings.

The precise mechanism behind the proposed method is still unclear. We presented a mathematical proof that the reconstructions convergence for *any* choice of α as the resolution is refined. Therefore, it remains an open question whether the unstable norms in Tables 1 would converge with higher resolutions, or if those numbers are inaccurate, reflecting the numerical instability arising from the ill-posedness of the underlying tomographic problem. In any case, in these real-data examples at least, the proposed method automatically adapts to the relevant resolution and actual noise level. This is very promising indeed.

The S-curve method, introduced in [35, 27], was found to work robustly and reliably for the present datasets. Curiously, the S-curve method produces parameter values of the same order of magnitude than the new resolution-based method. However, *a priori* information about the total variation of the unknown function is needed for applying the S-curve method, while the proposed multi-resolution based method does not need anything else than the data.

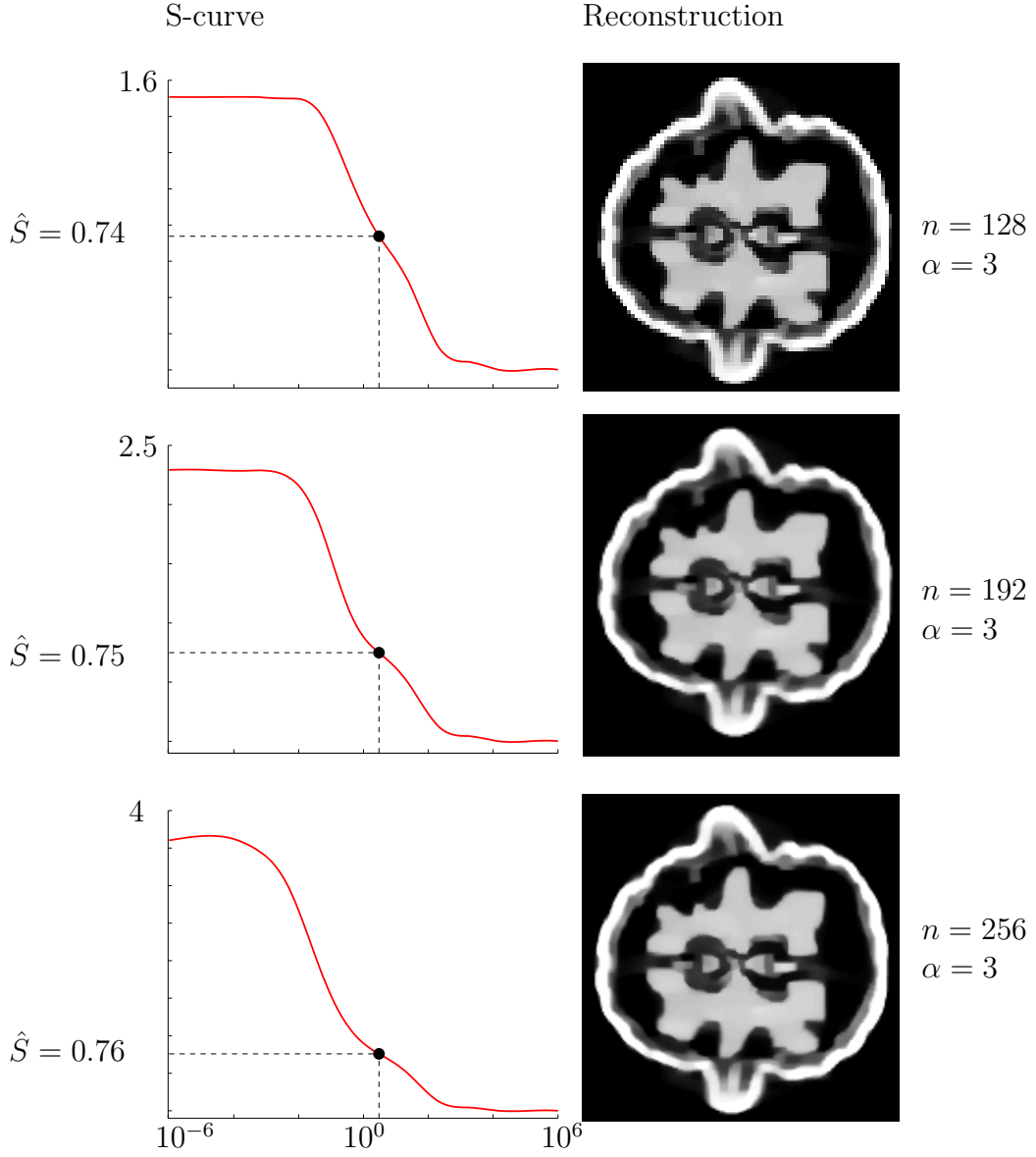


FIGURE 13. S-curve method applied to the measured projection data with no additional noise (case i). Left column: Plots of the S-curves used to determine the values of α . Right column: Reconstruction computed with the selected α .

The proposed method has the drawback that many reconstructions need to be computed with various choices of resolution n and regularization parameter α . This can be computationally demanding.

We stress that this work is just an initial feasibility study for the new parameter choice method. More comprehensive testing and comparisons to other methods are still needed to assess the properties of the new approach.

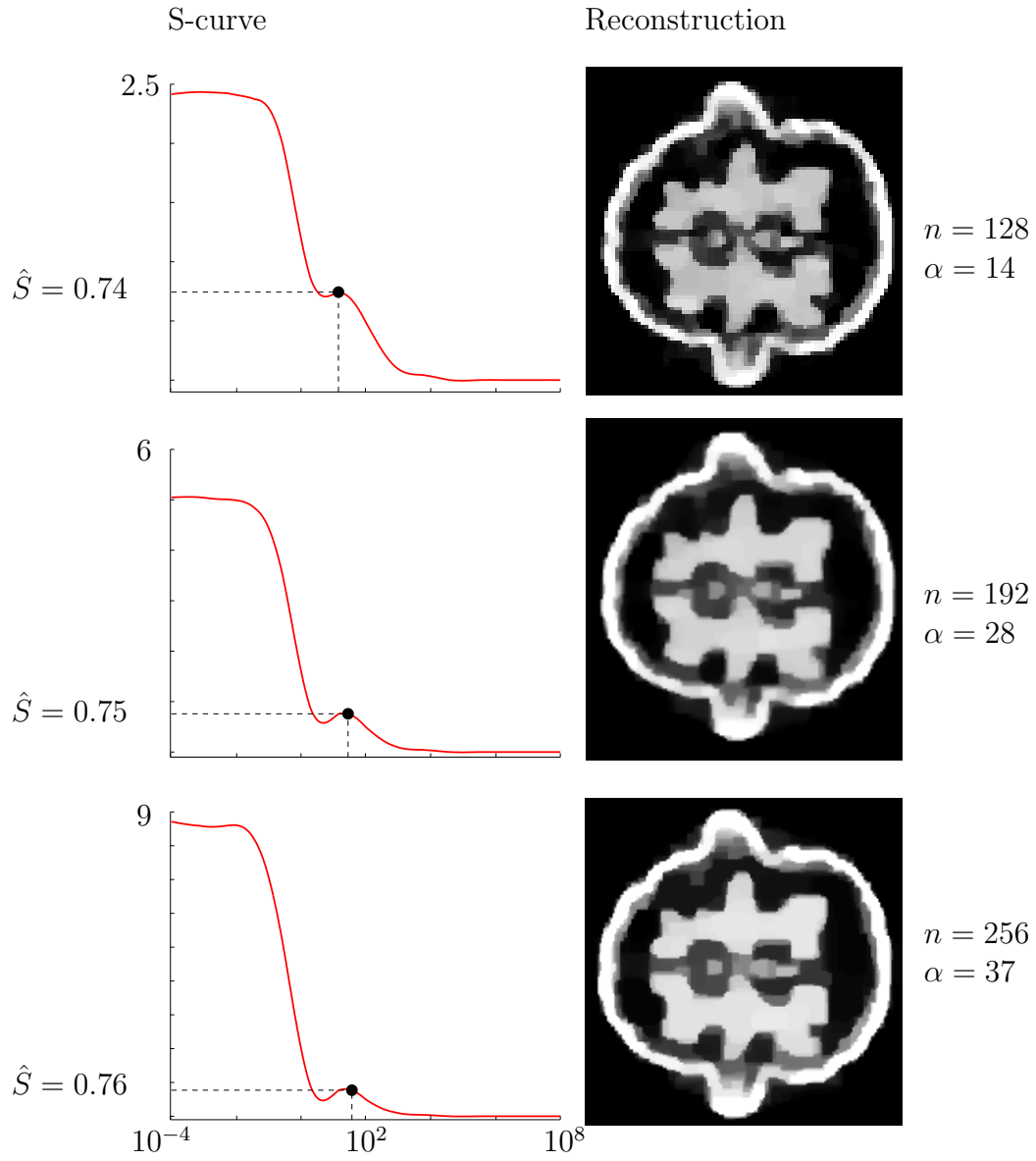


FIGURE 14. S-curve method applied to the measured projection data corrupted with 5% additional noise (case ii). Left column: Plots of the S-curves which were used to determine the values of α . Right column: Reconstruction computed using the selected α .

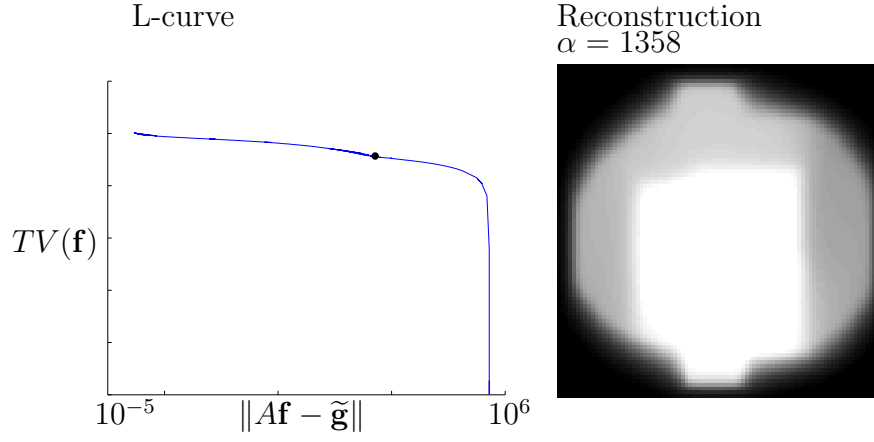


FIGURE 15. L-curve method applied to walnut data, no additional noise. Left: L-curve plot. Right: Reconstruction computed using the selected $\alpha = 1358$. The discretization level is $n = 128$.

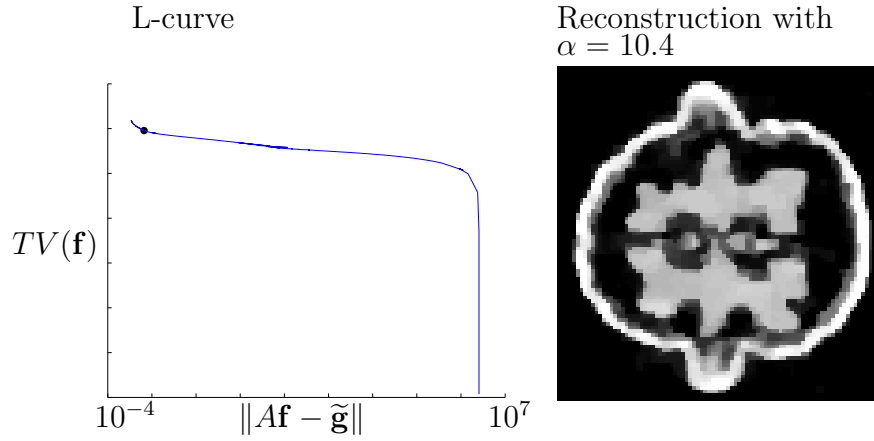


FIGURE 16. L-curve method applied to walnut data with 5% additional noise. Left: L-curve plot. Right: Reconstruction computed using the selected $\alpha = 10.4$. The discretization level is $n = 128$.

APPENDIX A. CONSTRUCTION OF THE DIFFERENCE MATRICES

Let us illustrate the construction of difference matrices D_H and D_V discussed in Section 4.2 with a simple example. Consider the 3×3 image matrix

$$\begin{bmatrix} f_{11} & f_{12} & f_{13} \\ f_{21} & f_{22} & f_{23} \\ f_{31} & f_{32} & f_{33} \end{bmatrix},$$

which is represented by the vector $\mathbf{f} = [f_{11}, f_{21}, f_{31}, f_{12}, f_{22}, f_{32}, f_{13}, f_{23}, f_{33}]^T \in \mathbb{R}^9$. Now the 9×9 horizontal difference matrix D_H takes the form

$$D_H = \frac{1}{n} \begin{bmatrix} -1 & 0 & 0 & 1 & 0 & 0 & 0 & 0 & 0 \\ 0 & 0 & 0 & -1 & 0 & 0 & 1 & 0 & 0 \\ 1 & 0 & 0 & 0 & 0 & 0 & -1 & 0 & 0 \\ 0 & -1 & 0 & 0 & 1 & 0 & 0 & 0 & 0 \\ 0 & 0 & 0 & 0 & -1 & 0 & 0 & 1 & 0 \\ 0 & 1 & 0 & 0 & 0 & 0 & 0 & -1 & 0 \\ 0 & 0 & -1 & 0 & 0 & 1 & 0 & 0 & 0 \\ 0 & 0 & 0 & 0 & 0 & -1 & 0 & 0 & 1 \\ 0 & 0 & 1 & 0 & 0 & 0 & 0 & 0 & -1 \end{bmatrix},$$

The construction of the vertical difference matrix D_V is similar.

APPENDIX B. A NOTE ON BV NORMS

What happened if one used the BV norm

$$\|u\|_{L^1(D)} + V_p(u) := \|u\|_{L^1(D)} + \int_D \left(\left| \frac{\partial u(x)}{\partial x_1} \right|^p + \left| \frac{\partial u(x)}{\partial x_2} \right|^p \right)^{1/p} dm(x)$$

with $p > 1$ in the analysis of Section 3? The norm (2.1) used there corresponds to the choice $p = 1$. First of all, taking $p > 1$ would only give an inequality in (3.12):

$$\lim_{j \rightarrow \infty} V_p(v_j) \geq V_p(u),$$

and the proof would not work.

Let us point out a specific example using $p = 2$. Consider the characteristic function $\chi = \chi_{\{|x| < 1\}}$ of the unit disc, whose BV norm is 2π : length of the boundary (which is 2π) times the jump (which is 1). Now approximate χ using functions equal to one inside pixel-based set approximations to the unit disc, see Figure 17. The total length of the boundary of each such set is 8. Thus the BV norms of the approximations converge to 8 instead of 2π .

Now using the BV norm with $p = 1$ leads to the (Manhattan) length of the unit circle to be 8, ensuring the appropriate convergence.

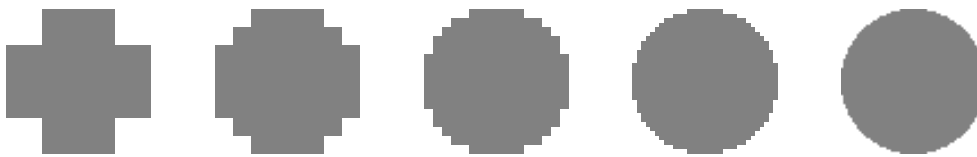


FIGURE 17. Pixel-based piecewise linear approximations to the characteristic function of the unit disc. Here white color denotes zero value and gray color denotes value one. The TV norm of all of these functions is exactly 8 (equal to the length of the boundary).

REFERENCES

- [1] H. ATTOUCH, G. BUTTAZZO, AND G. MICHAILLE, *Variational analysis in Sobolev and BV spaces: applications to PDEs and optimization*, vol. 17, Siam, 2014.
- [2] H. ATTOUCH AND R. WETS, *Epigraphical analysis*, *Analyse Non Lineaire (Annales de l'Institut Henri Poincare)*, 6 (1989), pp. 73–100.
- [3] S. BARTELS, *Total variation minimization with finite elements: Convergence and iterative solution*, *SIAM Journal on Numerical Analysis*, 50 (2012), pp. 1162–1180.
- [4] P. BĚLÍK AND M. LUSKIN, *Approximation by piecewise constant functions in a bv metric*, *Mathematical Models and Methods in Applied Sciences*, 13 (2003), pp. 373–393.
- [5] J. BIAN, X. HAN, E. Y. SIDKY, G. CAO, J. LU, O. ZHOU, AND X. PAN, *Investigation of sparse data mouse imaging using micro-CT with a carbon-nanotube-based X-ray source*, *Tsinghua Sci Technol*, 15 (2010), pp. 74–78.
- [6] J.-F. CAI, S. OSHER, AND Z. SHEN, *Linearized Bregman iterations for frame-based image deblurring*, *SIAM J. Imaging Sci.*, 2 (2009), pp. 226–252.
- [7] A. CHAMBOLLE, S. E. LEVINE, AND B. J. LUCIER, *An upwind finite-difference method for total variation-based image smoothing*, *SIAM J. Imaging Sci.*, 4 (2011), pp. 277–299.
- [8] T. F. CHAN AND K. CHEN, *On a nonlinear multigrid algorithm with primal relaxation for the image total variation minimisation*, *Numer. Algorithms*, 41 (2006), pp. 387–411.
- [9] T. F. CHAN, G. H. GOLUB, AND P. MULET, *A nonlinear primal-dual method for total variation-based image restoration*, *SIAM Journal on Scientific Computing*, 20 (1999), pp. 1964–1977.
- [10] T. F. CHAN AND J. SHEN, *Image processing and analysis*, Society for Industrial and Applied Mathematics (SIAM), Philadelphia, PA, 2005. Variational, PDE, wavelet, and stochastic methods.
- [11] R. CHARTRAND, E. Y. SIDKY, AND X. PAN, *Nonconvex compressive sensing for x-ray ct: An algorithm comparison*, in *Signals, Systems and Computers, 2013 Asilomar Conference on*, Nov 2013, pp. 665–669.
- [12] B. CHEN, M. YANG, Z. ZHANG, X. HAN, J. BIAN, E. SIDKY, AND X. PAN, *Constrained tv-minimization reconstruction from exterior ct data*, in *Nuclear Science Symposium and Medical Imaging Conference (NSS/MIC)*, 2013 IEEE, Oct 2013, pp. 1–3.
- [13] G. DAL MASO, *An introduction to Gamma-convergence*, Birkhäuser, 1993.
- [14] A. H. DELANEY AND Y. BRESLER, *Globally convergent edge-preserving regularized reconstruction: an application to limited-angle tomography*, *IEEE Transactions on Image Processing*, 7 (1998), pp. 204–221.
- [15] D. DOBSON AND C. VOGEL, *Convergence of an iterative method for total variation denoising*, *SIAM Journal on Numerical Analysis*, 34 (1997), pp. 1779–1791.

- [16] X. DUAN, L. ZHANG, Y. XING, Z. CHEN, AND J. CHENG, *Few-view projection reconstruction with an iterative reconstruction-reprojection algorithm and TV constraint*, Nuclear Science, IEEE Transactions on, 56 (2009), pp. 1377–1382.
- [17] H. ENGL, M. HANKE, AND A. NEUBAUER, *Regularization of inverse problems*, Kluwer Academic Publishers, 1996.
- [18] E. ESSER, X. ZHANG, AND T. CHAN, *A general framework for a class of first order primal-dual algorithms for convex optimization in imaging science*, SIAM Journal on Imaging Sciences, 3 (2010), pp. 1015–1046.
- [19] X. FENG AND A. PROHL, *Analysis of total variation flow and its finite element approximations*, ESAIM, Mathematical Modelling and Numerical Analysis, 37 (2003), pp. 533–556.
- [20] A. V. FIACCO AND G. P. MCCORMICK, *Nonlinear Programming: Sequential Unconstrained Minimization Techniques*, John Wiley and Sons, New York, New York, 1968.
- [21] M. FORNASIER, A. LANGER, AND C.-B. SCHÖNLIEB, *A convergent overlapping domain decomposition method for total variation minimization*, Numer. Math., 116 (2010), pp. 645–685.
- [22] M. FORNASIER AND C.-B. SCHÖNLIEB, *Subspace correction methods for total variation and l_1 -minimization*, SIAM J. Numer. Anal., 47 (2009), pp. 3397–3428.
- [23] D. GOLDFARB AND W. YIN, *Second-order cone programming methods for total variation-based image restoration*, SIAM J. Sci. Comput., 27 (2005), pp. 622–645 (electronic).
- [24] T. GOLDSTEIN AND S. OSHER, *The split Bregman method for L_1 -regularized problems*, SIAM J. Imaging Sci., 2 (2009), pp. 323–343.
- [25] E. T. HALE, W. YIN, AND Y. ZHANG, *Fixed-point continuation applied to compressed sensing: implementation and numerical experiments*, J. Comput. Math., 28 (2010), pp. 170–194.
- [26] K. HÄMÄLÄINEN, L. HARHANEN, A. HAUPTMANN, A. KALLONEN, E. NIEMI, AND S. SILTANEN, *Total variation regularization for large-scale x-ray tomography*, International Journal of Tomography & Simulation, 25 (2014), pp. 1–25.
- [27] K. HÄMÄLÄINEN, A. KALLONEN, V. KOLEHMAINEN, M. LASSAS, K. NIINIMÄKI, AND S. SILTANEN, *Sparse tomography*, SIAM Journal on Scientific Computing, 35 (2013), pp. B644–B665.
- [28] P. HANSEN, *Rank-Deficient and Discrete Ill-Posed Problems: Numerical Aspects of Linear Inversion*, SIAM, Philadelphia, PA, 1997.
- [29] P. C. HANSEN, *Discrete inverse problems*, vol. 7 of Fundamentals of Algorithms, Society for Industrial and Applied Mathematics (SIAM), Philadelphia, PA, 2010. Insight and algorithms.
- [30] G. T. HERMAN AND R. DAVIDI, *Image reconstruction from a small number of projections*, Inverse Problems, 24 (2008), p. 045011.
- [31] M. HINTERMÜLLER AND K. KUNISCH, *Total bounded variation regularization as a bilaterally constrained optimization problem*, SIAM J. Appl. Math., 64 (2004), pp. 1311–1333.
- [32] T. L. JENSEN, J. H. JØRGENSEN, P. C. HANSEN, AND S. H. JENSEN, *Implementation of an optimal first-order method for strongly convex total variation regularization*, BIT Numerical Mathematics, DOI: 10.1007/s10543-011-0359-8 (2011).
- [33] J. H. JØRGENSEN, T. L. JENSEN, P. C. HANSEN, S. H. JENSEN, E. Y. SIDKY, AND X. PAN, *Accelerated gradient methods for total-variation-based ct image reconstruction*, arXiv preprint arXiv:1105.4002, (2011).
- [34] S. KINDERMANN, L. D. MUTIMBU, AND E. RESMERITA, *A numerical study of heuristic parameter choice rules for total variation regularization*, Journal of Inverse and Ill-Posed Problems, 22 (2013), pp. 63–94.
- [35] V. KOLEHMAINEN, M. LASSAS, K. NIINIMÄKI, AND S. SILTANEN, *Sparsity-promoting Bayesian inversion*, Inverse Problems, 28 (2012), p. 025005.
- [36] V. KOLEHMAINEN, S. SILTANEN, S. JÄRVENPÄÄ, J. KAIPIO, P. KOISTINEN, M. LASSAS, J. PIRTTILÄ, AND E. SOMERSALO, *Statistical inversion for medical X-ray tomography with few radiographs: II. application to dental radiology*, Physics in Medicine and Biology, 48 (2003), pp. 1465–1490.

- [37] V. KOLEHMAINEN, A. VANNE, S. SILTANEN, S. JÄRVENPÄÄ, J. KAPIO, M. LASSAS, AND M. KALKE, *Parallelized Bayesian inversion for three-dimensional dental X-ray imaging*, IEEE Transactions on Medical Imaging, 25 (2006), pp. 218–228.
- [38] M. LASSAS AND S. SILTANEN, *Can one use total variation prior for edge-preserving Bayesian inversion?*, Inverse Problems, 20 (2004), pp. 1537–1564.
- [39] Y. LI AND F. SANTOSA, *A computational algorithm for minimizing total variation in image restoration*, IEEE Transactions on Image Processing, 5 (1996), pp. 987–995.
- [40] H. LIAO AND G. SAPIRO, *Sparse representations for limited data tomography*, in Biomedical Imaging: From Nano to Macro, 2008. ISBI 2008. 5th IEEE International Symposium on Biomedical Imaging, May 2008, pp. 1375–1378.
- [41] S. MEHROTRA, *On the implementation of a primal-dual interior point method*, SIAM Journal on Optimization, 2 (1992), pp. 575–601.
- [42] J. MUELLER AND S. SILTANEN, *Linear and Nonlinear Inverse Problems with Practical Applications*, vol. 10 of Computational Science and Engineering, SIAM, 2012.
- [43] F. NATTERER, *The mathematics of computerized tomography*, vol. 32, John Wiley & Sons, Chichester, USA, and B. G. Teubner, Stuttgart, Germany, 1986.
- [44] Y. NESTEROV, *Barrier subgradient method*, Math. Program., 127 (2011), pp. 31–56.
- [45] K. NIINIMÄKI, *Computational Optimization Methods for Large-scale Inverse Problems*, PhD thesis, University of Eastern Finland, 2013.
- [46] J. NOCEDAL AND S. WRIGHT, *Numerical Optimization*, Springer Series in Operations Research, Springer Verlag, New York, 2 ed., 2006.
- [47] S. OSHER, M. BURGER, D. GOLDFARB, J. XU, AND W. YIN, *An iterative regularization method for total variation-based image restoration*, Multiscale Model. Simul., 4 (2005), pp. 460–489 (electronic).
- [48] S. OSHER AND R. FEDKIW, *Level set methods and dynamic implicit surfaces*, vol. 153 of Applied Mathematical Sciences, Springer-Verlag, New York, 2003.
- [49] L. RUDIN, S. OSHER, AND E. FATEMI, *Nonlinear total variation based noise removal algorithms*, Physica D: Nonlinear Phenomena, 60 (1992), pp. 259–268.
- [50] O. SCHERZER, M. GRASMAIR, H. GROSSAUER, M. HALTMEIER, AND F. LENZEN, *Variational methods in imaging*, vol. 167 of Applied Mathematical Sciences, Springer Verlag, 2009.
- [51] E. Y. SIDKY, R. CHARTRAND, AND X. PAN, *Constrained non-convex tvp minimization for extremely sparse projection view sampling in ct*, in Nuclear Science Symposium and Medical Imaging Conference (NSS/MIC), 2013 IEEE, Oct 2013, pp. 1–3.
- [52] E. Y. SIDKY AND X. PAN, *Image reconstruction in circular cone-beam computed tomography by constrained, total-variation minimization*, Physics in Medicine and Biology, 53 (2008), p. 4777.
- [53] J. TANG, B. E. NETT, AND G.-H. CHEN, *Performance comparison between total variation (TV)-based compressed sensing and statistical iterative reconstruction algorithms*, Physics in Medicine and Biology, 54 (2009), p. 5781.
- [54] Z. TIAN, X. JIA, K. YUAN, T. PAN, AND S. B. JIANG, *Low-dose CT reconstruction via edge-preserving total variation regularization*, Physics in Medicine and Biology, 56 (2011), p. 5949.
- [55] C. VOGEL, *Computational methods for inverse problems*, no. 23, SIAM, Frontiers in Applied Mathematics, 2002.
- [56] C. VOGEL AND M. OMAN, *Fast, robust total variation-based reconstruction of noisy, blurred images*, IEEE Transactions on Image Processing, 7 (1998), pp. 813–824.
- [57] Y. WANG, J. YANG, W. YIN, AND Y. ZHANG, *A new alternating minimization algorithm for total variation image reconstruction*, SIAM J. Imaging Sci., 1 (2008), pp. 248–272.
- [58] Y.-W. WEN AND R. CHAN, *Parameter selection for total-variation-based image restoration using discrepancy principle*, Image Processing, IEEE Transactions on, 21 (2012), pp. 1770–1781.

- [59] S. WRIGHT, *Primal-Dual Interior-Point Methods*, vol. 54, SIAM, Philadelphia PA, 1997.
- [60] W. YIN, S. OSHER, D. GOLDFARB, AND J. DARBON, *Bregman iterative algorithms for l_1 -minimization with applications to compressed sensing*, SIAM J. Imaging Sci., 1 (2008), pp. 143–168.
- [61] X. ZHANG, M. BURGER, AND S. OSHER, *A unified primal-dual algorithm framework based on Bregman iteration*, J. Sci. Comput., 46 (2011), pp. 20–46.